Simulation of Sweep-Jet Flow Control, Single Jet and Full Vertical Tail

Robert E. Childs,* Paul M. Stremel,* Joseph A. Garcia,†
James T. Heineck,† Laura K. Kushner,† Bruce L. Storms†

I. Abstract

This work is a simulation technology demonstrator, of sweep jets used to suppress boundary layer separation and increase maximum achievable load coefficents. A sweep jet is a discrete Coanda jet that oscillates in the plane parallel to an aerodynamic surface. It injects mass and momentum in the approximate streamwise direction. It also generate turbulent eddies at the oscillation frequency, which are typically large relative to boundary layer turbulence, and which augmenting mixing across the boundary layer to attack flow separation. Simulations of a fluidic oscillator, the sweep jet emerging from the oscillator, and the suppression of boundary layer separation by an array of sweep jets are performed. Simulation results are compared to data from a dedicated CFD validation experiment of a single oscillator and its sweep jet, and from a study of a full-scale Boeing 757 vertical tail augmented with an array of sweep jets.[2,20] A critical step in the work is the development of realistic time-dependent sweep-jet inflow boundary conditions, derived from the results of the single-oscillator simulations, which create the sweep jets in the full-tail simulations. Simulations were performed using the Overflow CFD solver, with high-order spatial discretization and a range of turbulence modeling. Good results were obtained for all flows simulated, when suitable turbulence modeling was used.

II. Introduction

NASAs Environmentally Responsible Aviation (ERA) Project[1] explores concepts and technologies that have the potential to reduce aviation's adverse environment effects. The program covers topics in materials, airframe concepts, propulsion, and flow control. In the area of flow control, there are topics on natural laminar flow and boundary layer separation control. One such technology is the Active Flow Control (AFC) sweep jet, which can be used to delay boundary layer separation, increase the maximum aerodynamic loading, and enable the design of smaller and lighter structures with lower drag and fuel burn. Effective flow control may also be used to develop new air vehicle concepts, simplify existing ones and improve performance, for example. Many experimental studies have evaulated the use of sweep jets for flow control.[4,13,22] They have demonstrated the effectiveness of sweep jets at delaying stall on a lifting surface to higher angles of incidence, yielding higher maximum lift coefficients.

These sweep jets originate from an internal fluidic oscillator whose output flows through a converging-diverging nozzle, followed by a sharply diverging external nozzle, as shown in Fig. 1. All of the area in this Figure has full back wall (in the Figure's orientation); the oscillator, left of the right-most nozzle, also has a cover plate, making it an internal flow. High pressure steady air is supplied to the left-most passage, and unsteadiness develops within the loops of the oscillator, due to lagging negative feedback on the interior jet's angle. The instantaneous external jet does not diverge significantly; instead, it retains the nozzle's cross-section, approximately, and its flow angle oscillates between the two side-walls. This oscillating external jet is the sweep jet.

*Senior Research Scientist STC Corp.
†NASA, Ames Research Center

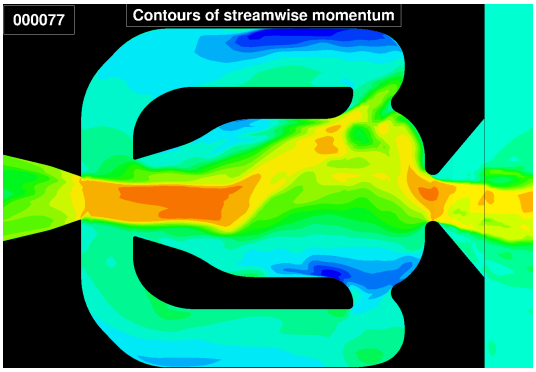

Figure 1: Streamwise momentum (left to right) in a fluidic oscillator and its near-field external jet. This image shows the central jet mid-way through flipping from top to bottom, forced by reversed flow in the top side feedback loop.

The sweep-jet AFC concept combines elements of a Coanda jet and of perdiodic forcing, which are both, independently, effective means of lift augmentation under some conditions. The effectiveness of sweep-jet AFC may result from multiple physical mechanisms. The oscillating jet generates rapid time-averaged spreading of the jet and elevated turbulent shear stress, in the plane of the oscillations. Less well understood is the nature of turbulence in the wall-normal direction, and how that turbulence interacts with the boundary layer and freestream above the sweep jet. The local freestream is the dominant source of energy available to energize the near-wall boundary layer, and hence delay separation. Thus, the interaction of the sweep jets with the outer flow may be significant in sweep-jet AFC performance.

The vertical tail on the Boeing 757 ecoDemonstrator is the focus of this study. On a modern twin-engine commercial transport aircraft, the vertical tail is sized to provide yaw loads in engine-out take-off scenarios, and it is over-sized for normal flight. System studies estimate that fuel consumption may be reduced by as much as few percent by using a smaller tail, made possible by AFC. The ecoDemonstrator tail is augmented with 38 sweep jets positioned in a uniform array just ahead of the rudder's starboard hingeline, which are intended to keep the rudder flow attached at high rudder deflection angles. (This test vehicle and tail are asymmetrical, using sweep jets to steer left.) The tail's performance was evaluated in a complex wind tunnel experiment conducted in the $40' \times 80'$ test section of the National Full-Scale Aerodynamics Complex (NFAC) operated by the Arnold Engineering Development Center (AEDC) at NASA's Ames Research Center. The augmented tail demonstrated enhanced side force in the wind tunnel test,[2,20] and flight testing was conducted by Boeing over the Strait of Juan de Fuca, in 2015.

The demonstrated success of sweep-jet flow control leads to a new challenge: how to develop good designs of products that use this AFC technology. At a time when the aerospace industry relies, increasingly and with good justification, on CFD-based design strategies, the aerodynamics of sweep-jet AFC are so complex that CFD accuracy and utility may be greatly diminished. Accurately simulating these highly unsteady sweep jets is challenging for CFD, and it was even thought to be unachievable by current CFD methods. The problem is very computationally intensive due to the highly unsteady AFC sweep jets and its induced turbulence, including the wide range of length and time scales of the turbulence in the mean flow.[3,6–8,13,14,17] If CFD is ineffective for sweep jet flows, this could force the design optimization work for all features associated with sweep-jet AFC back into the machine shop and wind tunnel, which will delay the adoption of this technology and its environmental benefits. Thus, the ability to simulate AFC aerodynamics is relevant to realizing the environmental goals of the ERA Program. While the main goal of this AFC wind tunnel test was to demonstrate the technology's effectiveness on the full scale tail, it also provides data for validation of simulation methods.

The work described here is a technology demonstration for simulations of sweep-jet AFC flows. The simulations encompass the entire relevant flow path of sweep jet aerodynamics, from "end-to-end," starting with inflow in a supply pipe upstream of the oscillator plenum and ending with the $40' \times 80'$ wind tunnel test section. However, this full range of length and time scale is not done in a single monolithic simulation. It is split into two parts: a single oscillator (and its near-field sweep jet), and the external domain of the full tail, starting from the sweep-jet nozzle throat. The nozzle-throat boundary conditions which power all of

the external flow sweep-jets are derived from the single-jet simulations, and they are very realistic. The decision to approximate sweep-jet inflow with boundary conditions (BCs) has important implications for the simulations' computational cost, accuracy and range of applicability, which are discussed below.

The three middle sections of this paper mirror these divisions in the simulation. One section involves CFD and measurements of a single oscillator and its sweep jet, in a dedicated wind tunnel experiment in the Fluid Mechanics Laborarory (FML) at NASA's Ames Research Center. The test involved an oscillator and sweep jet that were flight-scale (0.5″ across vertical, as viewed in Fig.1 and 0.25″ deep) and operated at supply pressures up to and exceeding the full-tail test. The next section covers the development and testing of the sweep-jet inflow BCs. These BCs consist of data extracted from the history from single-jet simulations, and boundary-condition software which "plays back" the recorded history, in the correct orientation, at the correct frequency, and onto the external-flow grid. The final section describes the results of using those BCs in the full Boeing 757 tail simulations, and compares simulation results to the data from full-tail wind tunnel test.

III. Simulation Methods

This section describes the relevant details of the CFD simulation methods. Simulations were performed using Overflow[16] version 2.2f on a system of overset structured grids, with grid connectivity generated by Pegasus.[15] The code was modified only to include an imposed-time-dependent boundary condition for the sweep jets.

Good spatio-temporal discretization accuracy is needed to resolve the relatively small scales and high frequencies of the sweep jets. Spatial discretization of the Euler terms was done with Overflow's fifth-order WENO-M scheme throughout all computational regions, except within a single grid zone at the base of the rudder where third-order was used to suppress numerical instability. Third-order upwind discretization was used for convection of turbulence variables, and second-order central differencing was used for diffusion terms, in all simulations. Time integration for all simulations was done using the "time-accurate mode" with inner iterations inside each time step. Flows that were intended to reach a steady state were run with first-order time integration, a large outer time step and a small number of inner iterations. This choice of parameters renders the simulations non-time-accurate, but they generally converge rapidly in a quasi-physical manner to a steady state. Flows that involved oscillating sweep jets were run with second-order integration, a suitably small time step, and enough inner iterations to achieve good inner-iteration convergence on integrated loads. The inner-iterative solver was the SSOR algorithm, with a spatially varying step and settings of $CFL_{min} \sim 10.0$ and $CFL_{max} \sim 25.0$. SSOR was also used for the turbulence model equations.

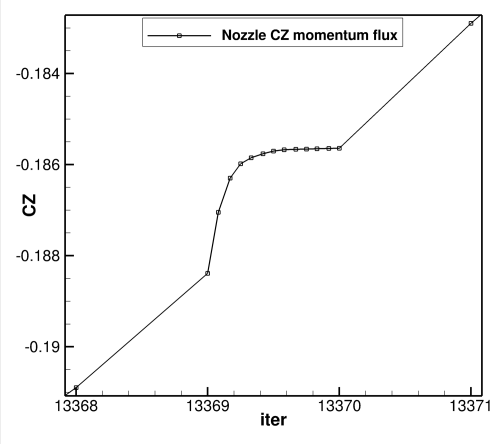

Figure 2: Example of the convergence of the sweep-jet nozzle throat lateral momentum flux coefficient (CZ) during the inner iterations of a time step (iter). The inner iteration must converge to its steady state to achieve intended outer-time-step accuracy. This level of inner-convergence is typical.

Conventional boundary conditions were used for all solid walls and the inflow/outflow planes in the wind-tunnel simulations. The sweep-jet inflow boundary conditions are discussed in their own section, below.

The choice of turbulence modeling is also important. Overflow has a range of turbulence modeling options, but this work considered only the SST-RANS[10,11] and SST-D/DES models. The flows studied here have distinctly different aerodynamics in different regions, and the use of zonal turbulence modeling was anticipated. It involves the use of different models in different regions of the flow, and requires a rational and empirically supported strategy for selecting the specific model to be used in each zone. Zonal turbulence modelling is easily accomplished in Overflow (within a family of models), by setting the "DES switch" appropriately in each grid zone. One part of the zonal strategy is to explicitly select the SST-RANS model where the flow

is expected to involve steady attached boundary layers. Where the flow may be separated or unsteady due to sweep jets, all of the RANS and D/DES options were treated as viable, to be judged in comparison to experimental measurements. The relative merits of these turbulence modeling options are discussed with the simulation results.

The grid spacing and time step have been refined, iteratively but not systematically, in response to the need perceived in prior less-refined solutions. Early in the work, qualitative grid refinement and time-step convergence studies were done with a single-jet simulation that involved both the interior oscillator and external jet. The grid refinement goal was to achieve 15 or more grid points across shear layers in critical regions of the flow (e.g., the central flow-path in Fig. 1) in RANS simulations. Because of shear layer dynamics, a relatively fine grid is needed across the oscillator's entire central flow-path. The same grids are used for RANS and D/DES simulations. A time step of $5\mu s$ was selected for the oscillator ans single sweep jet flows, based on a time-step study using the final grid system. The number of inner iterations was selected based on the inner-convergence of relavant integrated loads. The time-integration achieves its full outer time step accuracy only when the inner iterations converge to their asymptotic value. An example of sub-iteration convergence is shown in Fig. 2. The lateral momentum flux coefficient for the nozzle throat, which is the most important result of the single-jet simulations, is very close to its asymptotic value after twelve subiterations. Overflow's loads-integration was set to report the inner convergence infrequently (e.g. every 40^{th} time step), and this coarse running record of the inner convergence was reviewed occasionally throughout the work.

All sweep jets simulated in this work have the same physical dimensions, operate at comparable pressure ratios and Mach numbers, and have similar time scales. Thus, lessons learned in the single-jet work are relevant to the full-tail simulation. However, the full-tail simulations involve the far-downstream development of the sweep jets, where the dominant length scales are larger than in the oscillator and in the jet's near field.

IV. Single Oscillator and Sweep Jet

A critical part of the work has been the collaboration between simulation and experimental studies of a single sweep jet. This work was essential for establishing and validating CFD methods, and for developing the sweep-jet boundary conditions for the external-only flows. Experimental studies of the single sweep-jet were performed in the Fluid Mechanics Lab (FML) at the NASA Ames Research Center.[9] The single sweep-jet apparatus is shown in Fig. 3. The sweep jet nozzle is located far enough above the tunnel's bottom wall that the influence of the tunnel-wall on the near-field external jet is believed to be small. The primary experimental measurements used to assess simulation accuracy are the unsteady pressure at the nozzle throat, and PIV (particle imaging velocimetry) of the exterior sweep jet. Schlieren images provide a qualitative comparison of the instantaneous external jet structure.

The flow conditions for this test typically involved a freestream Mach number of $M_\infty = 0.15$, with jet plenum pressures up to $48psig$. Many of the measurements were taken at a plenum pressure of $38psig$ and $M_\infty = 0.15$, as conditions near this value had performed well in the test of the full-tail, and the single-jet CFD simulations focused on this case. At a supply pressure of $38psig$ and with modest internal losses, the external sweep jet is supersonic.

A brief review of the physics of the fluidic oscillation is relevant to guiding decisions about how to best run the simulations. Figure 4 gives four frames from a movie, and illustrates one half of an oscillation period. In the first frame, the central jet has just become attached to the upper wall of the central passage. The impact of the jet on the upper right corner of the central passage, drives higher pressure and reversed flow in the upper side-loop, as seen in the second frame. In the third frame, the reversed flow gains strength, which in turn forces the central jet away from the upper wall, and toward to lower wall of the central passage. The last frame shows the central jet attached to the lower wall, and it is essentially a mirror image of the first frame. This description is principally one of inviscid incompressible convective fluid dynamics. The acoustic propagation time is roughly an order of magnitude faster than this convective process. It is probable that turbulent entrainment of fluid between the central jet and an adjacent wall plays a significant role when the two are in proximity. Entrainment will help the central jet stick to the closest wall, and turn the corner into

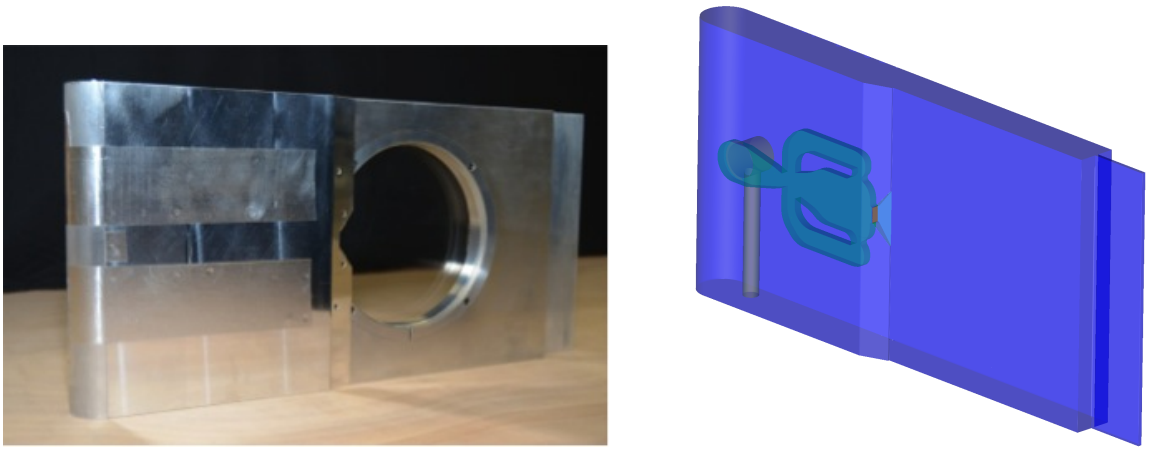

Figure 3: Photograph of single sweep jet test article (left), and see-through image of CFD surface definition (right). Jet air supplied via a pipe through the tunnel floor. Sweep jet nozzle is in the "notch" at the left edge of the window that provides PIV and Schlieren access. External flow is from left to right. A trailing edge splitter plate stabilizes the downstream wake flow.

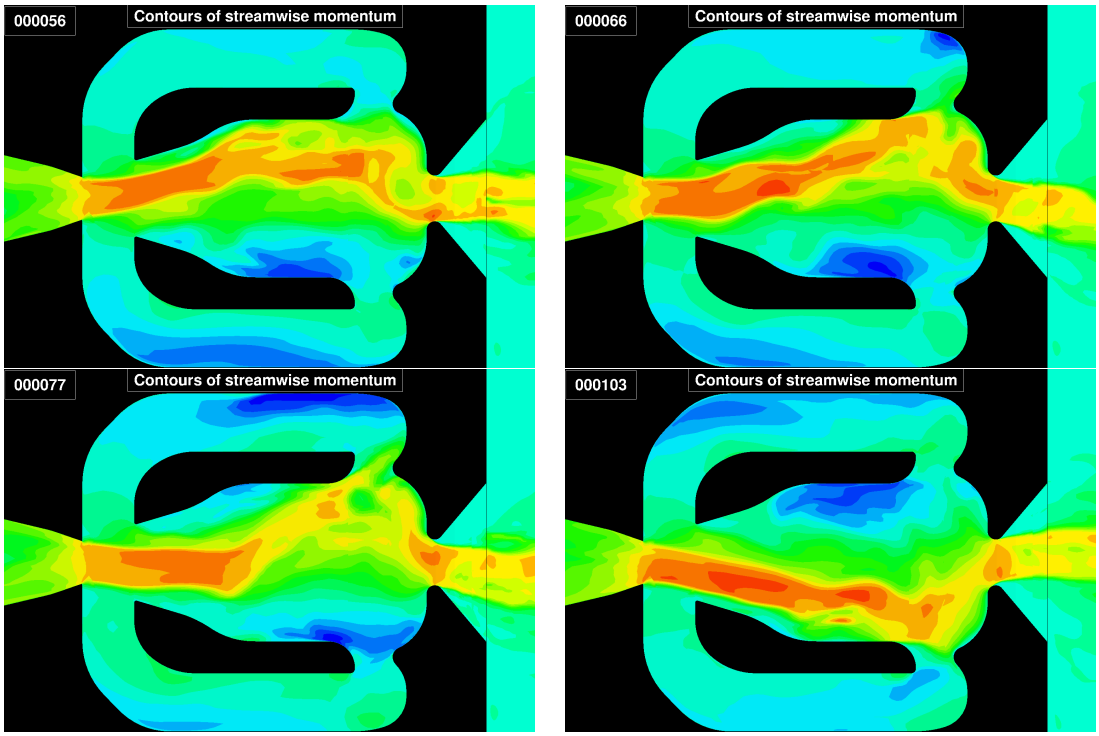

Figure 4: Streamwise momentum in fluidic oscillator and near-field external jet in a time sequence (frame number in upper left corner) during a half period of oscillation. Supply pressure is steady $38psig$. Images are from CFD, with DES turbulence modeling. Primary flow is from left to right (red contours) in central passage, while reversed flow (blue contours) occurs in central passage and side-loops. Observe the mirror-image phase reversal of the central-jet and reversed flow in side-loops between the first and last frames.

the side-loop. One can speculate that this will help energize flow into the side loops, and delay the central jet releasing from a wall due to forcing from the side-loop flow.

This disussion, partly speculative, suggests that viscous and invisid mechanisms are important in the central passage, while inviscid mechanisms dominate flow in the side-loops. Therefore, the central passage must have a fine enough grid to support accurate resolution of the central jet's shear layers, and the modeling of turbulence and its entrainment are important. The oscillator interior grid (Fig. 5) was repeatedly refined

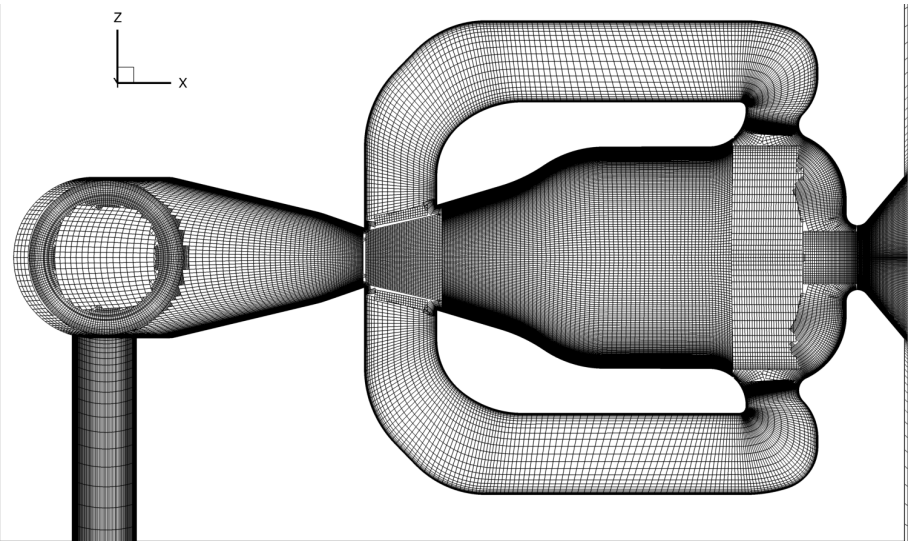

Figure 5: Grid used in oscillator. The grid used for the results presented here had 36M grid points, with about half of those used for the oscillator flow.

until the solution appeared to be adequately resolved, with ~ 15 grid points across the central jet's shear layers in RANS simulations. Because of its special grid-converge properties, DES simulations were not judged in this manner.

Figure 6 gives three images of the instantaneous jet field, selected "by eye" to be approximately at the same phase. The jet supply pressure is $p_s = 38psig$ for all three images. The PIV and CFD velocity data have freestream Mach number $M_\infty = 0.15$ The RBOS image (retroreflective background-oriented Schlieren) from Kushner[9] has $M_\infty = 0$ to mitigate blurring from tunnel vibration. Key features to note in these images include: (1) the similarity of the shape of the jet's arc, (2) the tendency to have a compact near-field jet and a spreading downstream jet, (3) CFD and RBOS show about 5 shock cells, while shock cells are not visible in the PIV data, (4) PIV exhibits higher velocity outside of the jet, relative to CFD. The comparison of instantaneous flow images can only suggest qualitative similarity, as there are significant cycle-to-cycle differences in the flow. Kushner[9] also compared CFD and experimental mean flow images, but these are also qualitative.

High-frequency pressure data from near the nozzle exit were used to assess the accuracy of the oscillator interior simulations and to select the turbulence modeling for the interior flow. A Kulite pressure port located adjacent to the upper side-wall of the nozzle throat (0.045″ downstream 0.219″ offset from the center of the throat) was selected for the highest-frequency Kulite measurements, because it reflects interior processes and the initial exterior deflection of the sweep jet, which is critical to the exterior flow. The CFD image in Fig. 6 includes pressure contour lines, and the pressure at the Kulite port is elevated when the jet is deflected toward the upper wall. The Kulite signal was obtained at $100kHz$ and then passed through a $25kHz$ low-pass filter. Simulations of the interior were run using the SST RANS and the SST DES models. The CFD time step was $200kHz^{-1}$ and the sampling rate was $100kHz^{-1}$. It is estimated that signals below $\sim 10kHz$ are very well resolved, based on the properties of the time integration.

Figure 7 compares the measured and simulated pressure histories. The CFD time was adjusted to align the phase with the experiment, as absolute time is irrelevant, and the sample period is representative: these images give neither the worst nor best comparisons that might be found throughout the full time records. The left image gives the pressure history for the RANS simulation over ~ 8 periods, while the right image gives DES results over ~ 3 periods. Four characteristics of the pressure signals are noted. (1) There is significant cycle-to-cycle variability in the period and amplitude of the pressure signal, in both CFD and experiment. (2) There is good net phase agreement over the full interval is this figure, as the pressure rise at $t = 0.101$ and $t = 0.131$ shows good coincidence between CFD and experiment. Spectra given below also demonstrate good accuracy for the dominant frequency. (3) The CFD pressure fluctuation amplitude is noticeably lower than the experiment. The strength of the pressure signal exhibits strong dependence on

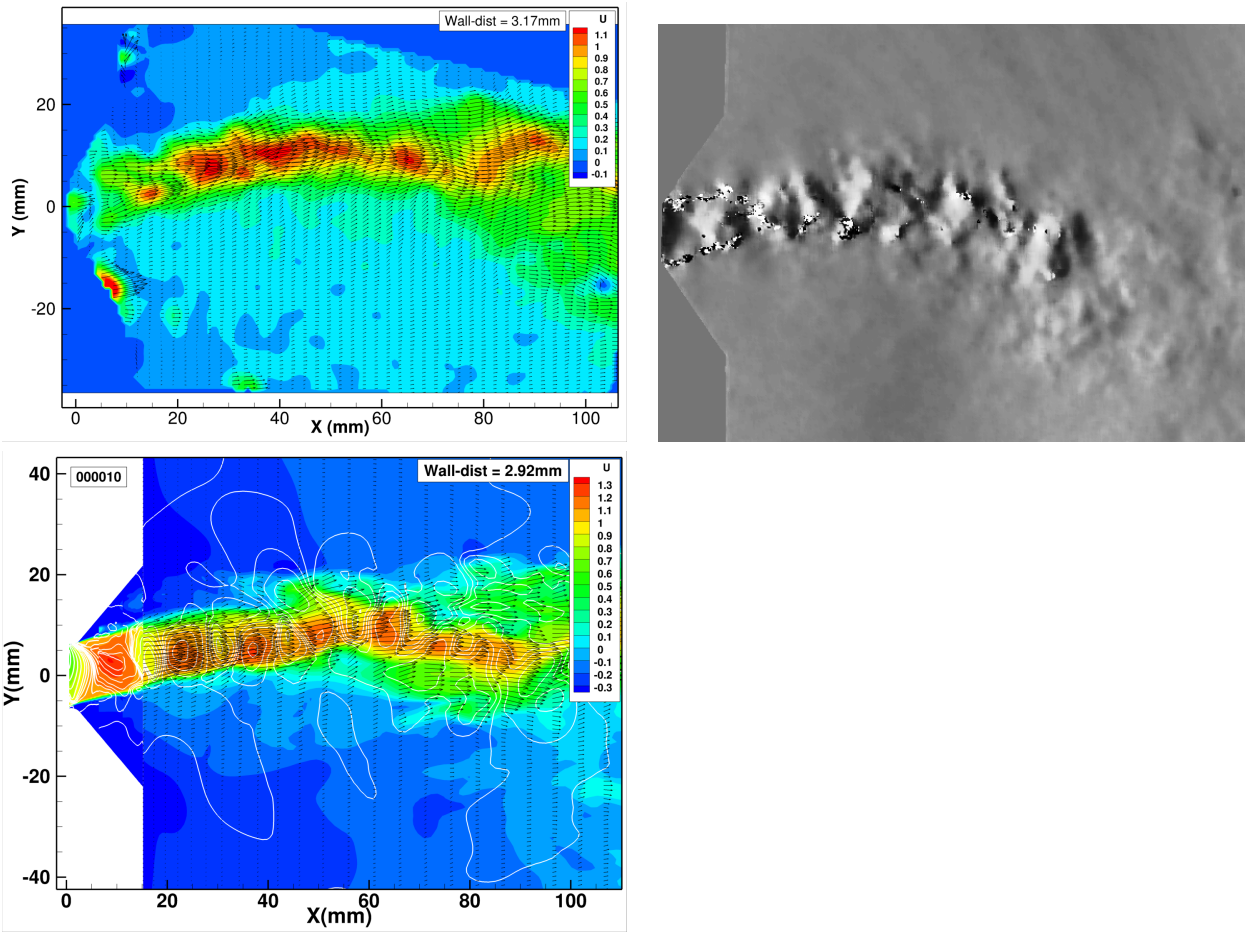

Figure 6: Visualization of instantaneous sweep jet at jet $p_s = 38psig$. Experimental PIV and Schlieren images, top row; Simulation with RANS modeling for interior flow and DDES for exterior flow. Flood color contours of streamwise velocity U, normalized by sound speed $c = 335m/s$; velocity vectors; white line contours of pressure in CFD results. Jet phase was selected for approximate similarity in all images.

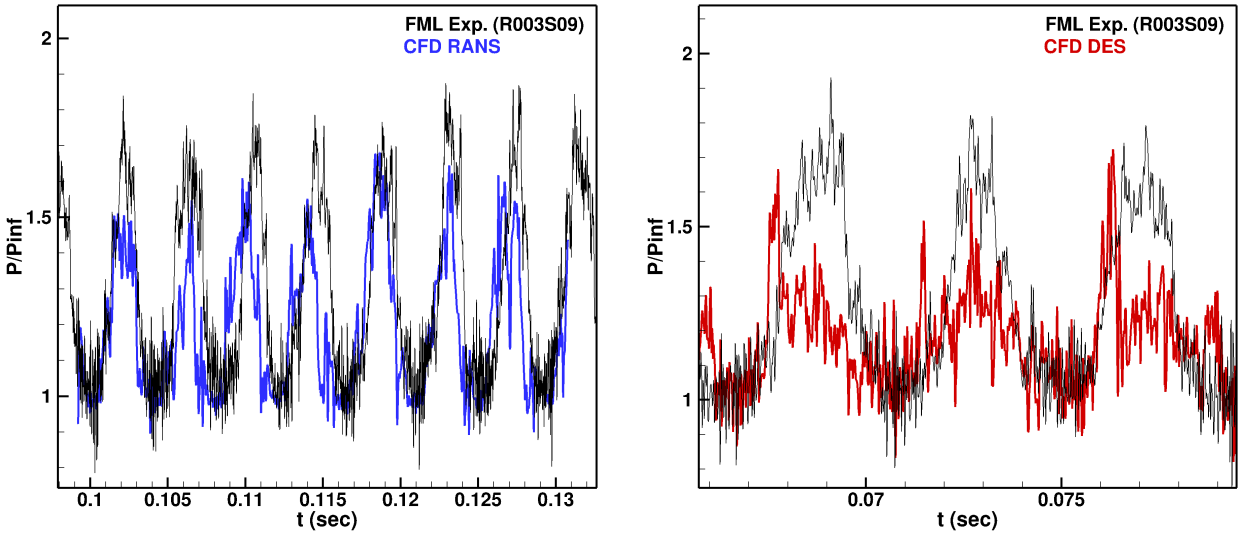

Figure 7: Time history of P/P_∞ from FML Kulite measurements at the side-wall of the nozzle throat, from RANS and DES simulations.

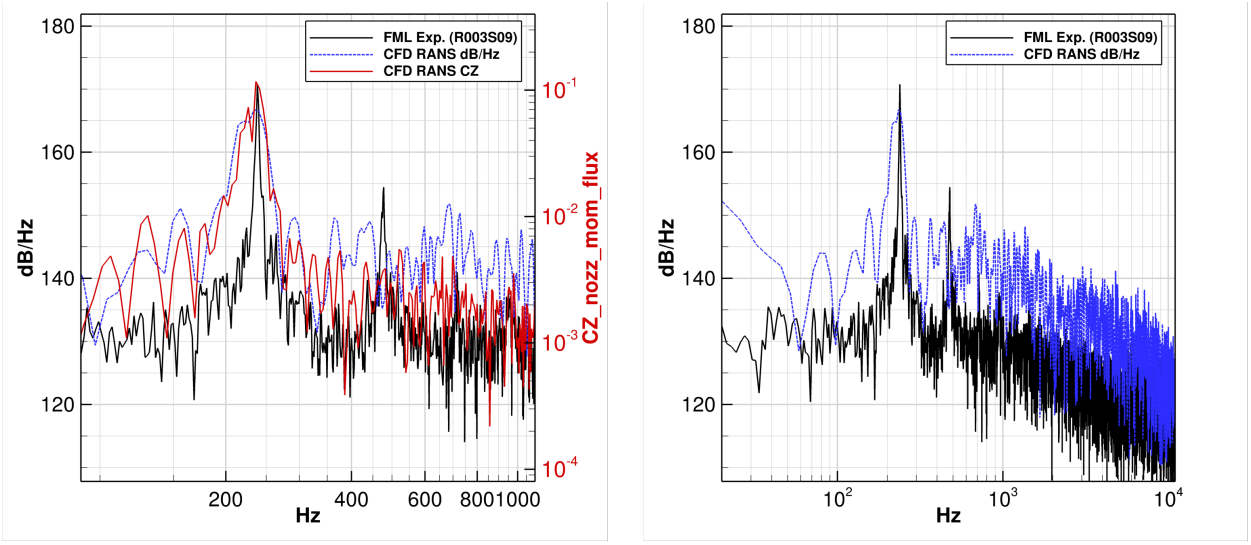

Figure 8: Spectra of nozzle throat pressure, measured in FML test and CFD, and CFD throat momentum flux coefficient (see text). Details near peak in spectrum, left, and full resolved spectrum, right.

turbulence modeling, with the RANS simulations being superior to DES for this pressure comparison. (4) The shape of the RANS and experimental pressure signals have many similarities: both dwell longer at low pressure and spends less time at high pressure, they have relatively rapid transitions between low and high pressure, and the qualitative nature of the high-frequency "jaggedness" in the signals is similar.

Several characteristics of the DES results are inferior to the RANS results. While the peak-to-peak pressures are comparable to RANS results, those peaks are reached by pressure fluctuations at frequencies well above the dominant frequency, and there is too little energy in the dominant frequency. Also, the character of the waveform differs from experiment and RANS: the large, rapid transition events between low and high pressure are generally absent; in their place is a weaker oscillation at the primary frequency plus significant high-frequency energy. However, the DES short-time peak-to-peak pressure signal better matches the experiment, when the signal is dwelling near $P/P_\infty = 1$. For simulations of the full tail, we expect that the strength of the signal at the dominant frequency is of greatest importance, and that the RANS oscillator simulation is preferred.

Spectra from experiment and CFD are shown in Fig. 8. This Figure compares spectra of the measured and simulated pressures, and the nozzle throat lateral momentum flux which is directly related to the jet sweep angle. The experiment has a narrow primary peak at $f_1 \sim 238Hz$ and harmonics at $f_2 \sim 475Hz$ and $f_3 \sim 710Hz$, which are down $\sim 16dB$ and $\sim 30dB$ respectively from the primary peak. The pressure spectrum from RANS-CFD interior simulation appears to have two essentially merged peaks at $\sim 220Hz$ and $\sim 238Hz$. At one time in the work, the $\sim 220Hz$ appear to be the dominant one, and some subsequent analysis was perfomed using that period. Also included is the spectrum of the nozzle's z-momentum flux coefficient, CZ, which has a better defined peak at $\sim 238Hz$. (The CZ amplitude was *artificially* matched to the experimental PSD to help see the peak in the spectrum.) One of the challenges in spectral analysis of CFD results is the very long run times that are needed to obtain good frequency resolution. The frequency resolution in the experimental data is $\sim 1.5Hz$. The CFD simulation ran for total duration of $\sim 0.2s$, and the best possible resolution of the spectra is $\sim 5Hz$. That resolution is available only in the integrated loads, which were recorded from the start on the simulation. Due to the Hamm windowing $(1 - cos)$, the start-up transient is strongly deemphasized from the spectrum; a side effect of windowing is some degradation of the actual frequency resolution. The CFD pressure data needed for comparison with the Kulite data were recorded for roughly the last 75% of the total simulation, and have a precision of $\sim 7Hz$, which is further degraded by windowing. The higher harmonic peaks seen in the experimental data do not appear in the CFD results.

The accuracy of the exterior flow simulation is judged by comparison to PIV measurements of the mean and averaged fluctuating velocities, in the area above the glass window shown in Fig. 3. This flow is difficult

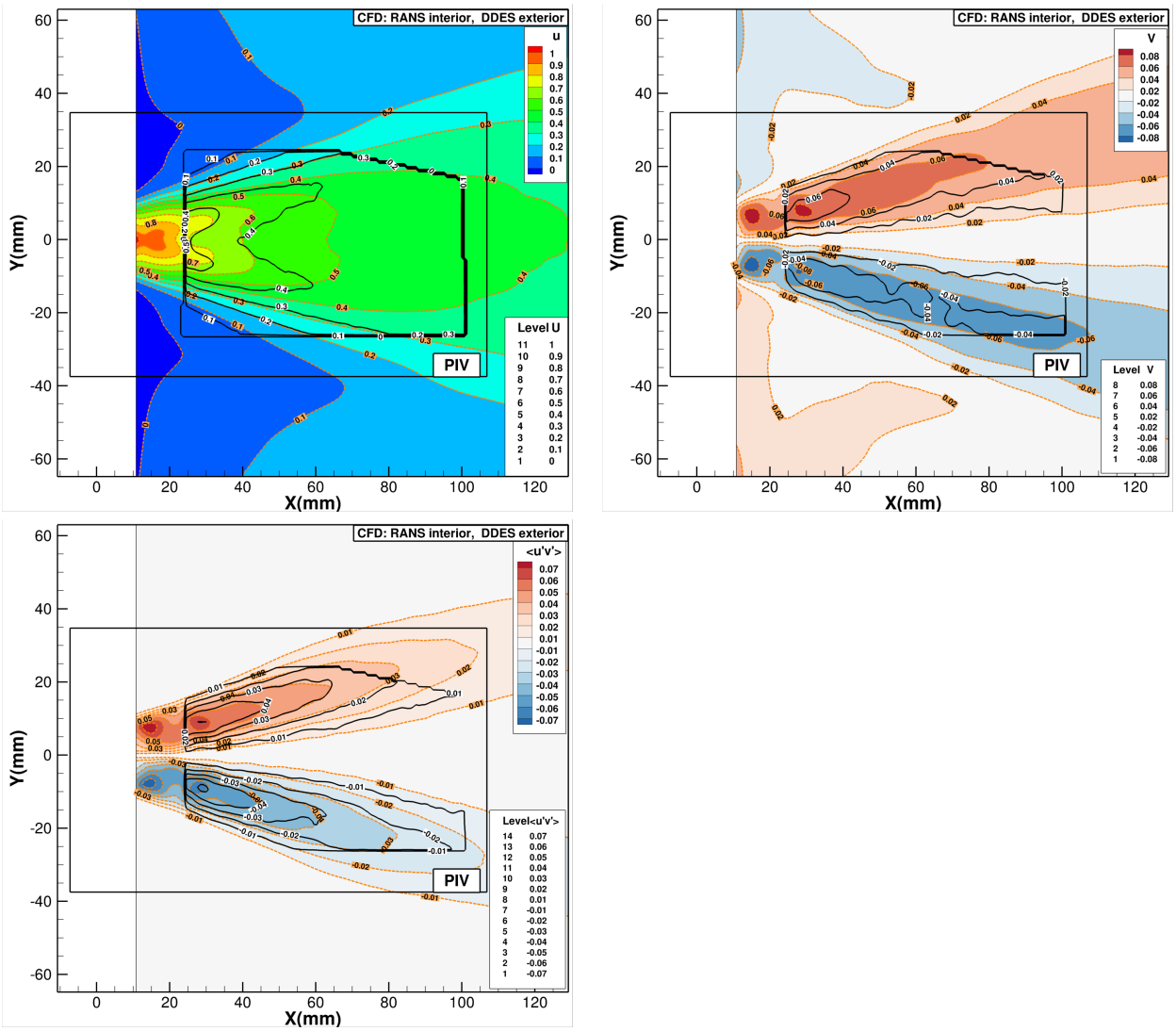

Figure 9: Comparison of simulation and PIV measurement of FML sweep jet. Plot origin $(0, 0)$ is at center of jet nozzle. CFD is color flood contours, with orange lines and label. Heavy black lines inside "PIV" box are PIV measurement data. Plot legends indicate variables: mean U and V, and turbulent shear stress $\overline{u'v'}$. Velocities normalized by sound speed, $335m/s$. (Truncated PIV contours on periphery are due to a limited field of view.)

to measure with PIV due in part to the wide range of velocities and the potential for glare from adjacent surfaces. Fig.6 illustrates that PIV did not acquire consistently useful data in the jet's near-field, as the jet should appear approximately similar to that shown in CFD and Schlieren images. Figure 9 gives plots of the mean streamwise and cross flow velocities, U and V, and the turbulent shear stress, $\overline{u'v'}$, which is the vertical transport of the streamwise momentum, in the frame of the figure, which compare CFD and PIV results. Velocities are normalized by the freestream sound speed $c = 335m/s$. The simulation uses RANS turbulence modeling inside the oscillator and DDES modeling for the exterior flow. The PIV measurement plane is nominally $1mm$ wide, centered in the jet throat and thus $3.175mm$ $(1/8'')$ from the wall. The PIV data are captured on an array of 148 data-reduction sites. The CFD data are from the grid plane $2.92mm$ from the wall, which is the closest to the center of the measurement plane, of the planes recorded during the simulation. The CFD shear stress includes the resolved turbulence, plus the stress modeled using the strain rate and eddy viscosity.

Several features of the PIV and CFD are in good agreement, but there are also notable differences. The mean streamwise velocity U exhibits good agreement at the outer edge of the jet, although the PIV data show the

jet to more spread-out than the CFD, by a small amount. Both PIV and CFD exhibit two U maxima in the jet's core region, which result from the the sweep-jet "pausing" briefly at maximum deflection, as suggested in the throat Kulite pressure signal. Again there are differences in the details of these two maxima, and significant differences in the velocity magnitude; at the minimum x where there is PIV data, the CFD $U_{max} \sim 0.75$, while for PIV $U_{max} \sim 0.55$, so PIV is roughly $\sim$30% below CFD. The mean vertical velocity V also shows good overall similarity in the shape of the jet, with the CFD results roughly $\sim 30\%$ higher than PIV data. The peaks in the $\overline{u'v'}$ shear stress, both positive and negative, tend to align with the region of maximum strain rate in the jet's mean flow, and thus indicate the spreading angle of the jet. Simulation and PIV agree well on this spreading angle. The maximum magnitude of the shear stress, inside the PIV window, is $|\overline{u'v'}|_{max} \sim 0.06$ for CFD, compared to $|\overline{u'v'}|_{max} \sim 0.05$ in the PIV data. Both CFD and PIV also exhibit small local peaks in the shear stress magnitude at $x \sim 27mm$, which is spatially associated with the shock cells seen in Fig. 6.

In general, the CFD simulations capture the main features of this single sweep-jet flow very well, most importantly, the dominant frequency and spreading rate of the sweep jet. Pressure histories at the nozzle throat lead to the selection of SST RANS modeling for the interior of the oscillator. The SST DDES model is favored for the exterior flow based principally on the anticipation that separation from the rudder will largely determine the accuracy of the global tail simulation. The results shown here suggest that DDES is suitable for the near-field external flow, but nothing yet can be stated about the far-downstream region, or about modeling accuracy in the presence of an adverse pressure gradient.

V. Unsteady Sweep Jet Boundary Conditions

The recorded history of the flow at the throat of the single sweep jet is used to create highly realistic sweep-jet inflow boundary conditions for the external flow; this provides consistently reproducable jet behavior and greatly reduces computational cost, at a small penalty in reduced realism of the full simulation. The benefits and validity of the using unsteady nozzle throat boundary conditions (BCs), and the processing steps used to create the BCs, are described in this section.

This "external-only" strategy for the full-tail simulations has two significant benefits. One benefit is to reduce computational cost. The single jet simulation was run using $\sim 18M$ grid points for the oscillator interior, so 31 similar oscillators would have required $\sim 550M$ grid points. In comparison, the grid for the exterior-only simulation of the full tail has $\sim 220M$ grid points. If all oscillators were included in the full-tail simulations, they would have accounted for $\sim$70% of the total grid points, with direct implications for computational cost. Using the unsteady throat BCs makes that part of the computational cost essentially zero. The second benefit is to provide control over the sweep jets. Both the experiment and single-jet simulations of the single jet had occasional random "hiccups," in which the throat pressure oscillation was much different than normal. While this may be physical, it could adversely affect a very long and expensive simulation. This behavior was avoided in selecting the jet history to supply the boundary conditions. Also, the phase, frequency and strength of the sweep jets can be explicitly adjusted, within some limits, to model the external effects of slightly different oscillator conditions.

The validity of powering the external sweep jets with unsteady nozzle throat BCs is affected by several flow-physics and algorithmic considerations. This topic was addressed only briefly in the present work, as the focus was on completing the full-tail simulations; it deserves further study to help advance the sweep-jet flow control technology. A key flow-physics issue is whether the external flow can influence the internal flow. If the nozzle throat flow is choked, the oscillator interior flow is isolated from the exterior, and the nozzle-throat boundary conditions can be highly accurate. The single-jet simulations discussed here involve jet supply pressures of $38psig$, exhausting to atmospheric or lower pressures, which yields choked *mean* flow. However, there are small near-wall regions of reversed flow at the nozzle throat, as seen in Fig 6, even if the main flow is choked. In some applications, even lower pressure jets may be used, in which the external pressure clearly affects the interior flow. Thus, the relevant concern is the level of outside influence that flows upstream into the oscillator, as a function of the gross mean parameters at the nozzle, such as its pressure ratio. The cases considered here involved oscillator plenum pressures which exceeded that needed to choke the mean nozzle flow, and we do not here attempt to address issues that arise from mean subsonic flow at the nozzle throat. No problems were encountered using the nozzle-throat boundary conditions.

The key steps in implementing the nozzle-throat BCs are summaried here, and some additional details are given below.

1. A single-jet simulation is run at approximately the correct pressure pressure ratio until it reaches its asymptotic unsteady state.
2. The flow history is recorded at the plane of the nozzle throat over many oscillation periods .
3. A time-interval consisting of a small integer number of oscillation periods is selected for the boundary conditions, base on the data's good native periodicity. This is a 3D data set consisting of two space dimensions and time, containing all simulation variables.
4. The flow in the selected time-interval is "regularized" to make it fully periodic and without reversed flow.
5. The flow is rotated to the orientation of the installed nozzles on the full tail.
6. Spatial interpolation is used to transfer the single-jet simulation data onto the grid points of the full-tail simulation, as the grids differ in the present work.
7. Minor scaling in the nozzle mass-flux and pressure have been applied in some cases, to model supply pressures and mass-flow rates different from the single-jet simulation.
8. A specialized time-dependent boundary-condition routine selects the appropriate time in the boundary data, based on physical time and sweep-jet frequency, and the phase of the individual sweep jet, and applies that data to the nozzle boundary plane in the CFD solution.

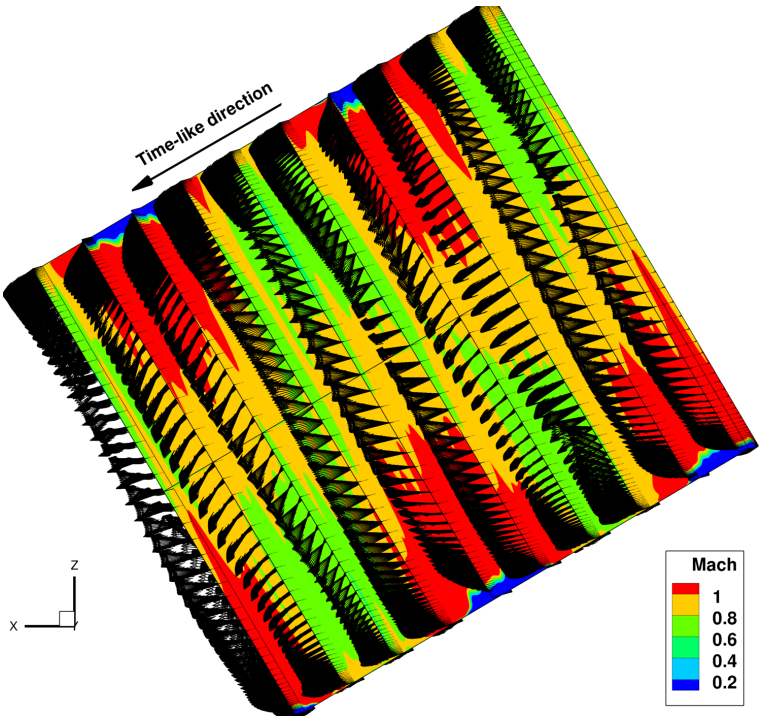

Figure 10: Visualization of the nozzle throat boundary condition data file, which includes two dominant periods in the time-like direction. Note that this is x-y-z-t data rendered on an x-z plot. Color flood contours of Mach number are given on the centerplane and at selected planes in time-like direction. Velocity vectors are visible above the centerplane and they illustrate the variation of the flow in the plane that becomes the instantaneous throat velocity field. The instantaneous boundary conditions are extracted on a plane perpendicular to the time-like direction, that advances in the time-like direction.

The nozzle-throat inflow BCs must be representative of the true flow and purely time periodic, so it can be repeated seamlessly and endlessly, for as long as needed for the exterior flow to reach statistical convergance. The native recorded nozzle throat history does not meet this requirement. The oscillator flow considered here has a strong dominant peak in its energy spectrum, but it also has significant energy outside that spectral peak. The first step in processing the native nozzle throat data is to find an integer number of periods, N,

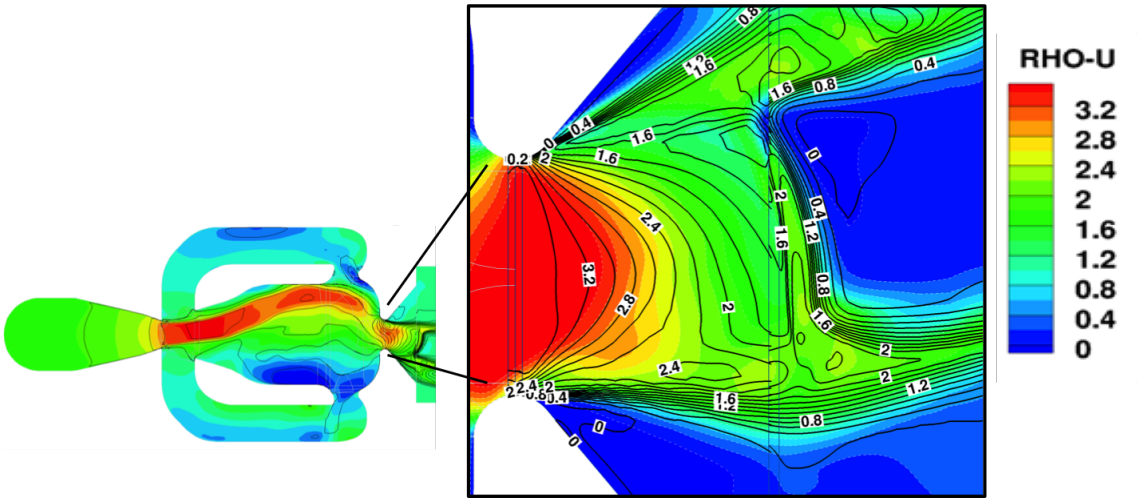

Figure 11: An overlay of contour plots of the streamwize momentum from the full interior-exterior sweep-jet solution (color contours) and from the exterior-only solution powered by throat boundary conditions (black line contours) demonstrate goods agreement downstream of the nozzle throat.

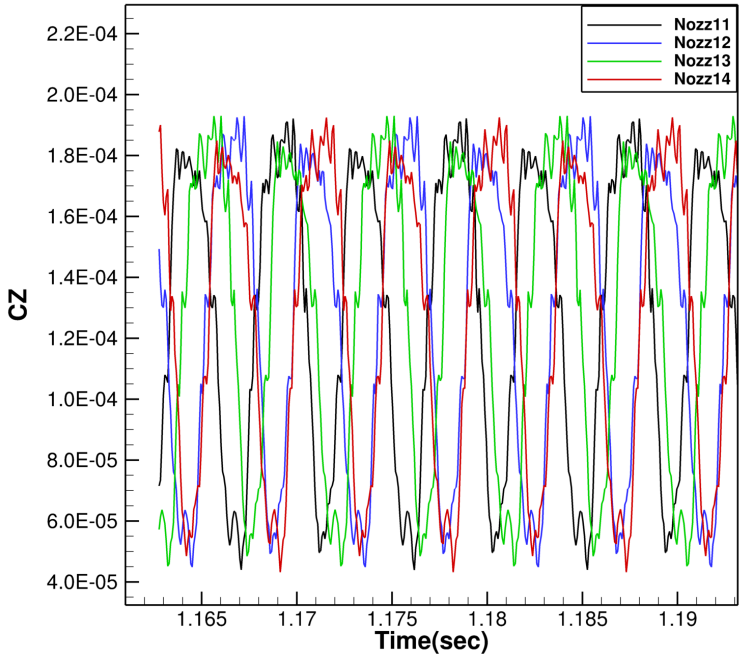

Figure 12: The vertical momentum flux coefficient, CZ, of 4 adjacent nozzles, numbered 11 through 14, in a full-tail simulation powered by sweep-jet boundary conditions.

that has small non-periodicity. A search algorithm was constructed that measured the RMS difference in the solution and its first and second time derivatives at integer oscillation periods, in which the period was determined by Fourier analysis of the throat lateral momentum flux over the full asymptotic solution history. Then, the non-periodicity is removed from this history. The native data are discontinuous at the ends of the N-period record. This discontinuity can be represented as a mean slope, which is subtracted from the data, which distributes the native non-periodicity over the full N-period record and gives C^0 periodicity. Increasing the number of cycles included in this BC record reduces this distributed error, at any point in time. In the small regions of instantaneous reversed flow, the velocity was set to zero, and the pressure and density were unchanged. The final step in achieving periodicity is to lightly smooth the flow variables with mixed second and fourth-order smoothing that respected periodicity in the time-like direction. The rotation and interpolation onto the orientation and grid spacing of the sweep-jet nozzle of the full-tail grid system

are mathematically straightforward. The result of this processing is a 3D data set, of two space dimensions and time, representing a time interval that is an integer multiple of the dominant oscillator period.

A graphic representation of the BC data file used by Overflow for the full-tail simulations is given in Fig. 10. For this illustration, the time-like direction has been converted into an artificial space dimension, normal to the plane of the nozzle, which is oriented as in the full-tail simulations. Two dominant periods of the jet oscillation are present in the data, as seen by the two patches each of low and high Mach number on the upper edge. (The lower edge has two similar patches, but one of these is split by the periodic boundary, at the ends of the time-like direction.) Significant cycle-to-cycle variation in the details of the contours can be seen between the two cycles.

The ability to alter the available nozzle throat boundary condition data to match a specific operatining condition enhances the flexibility and utility of the this jet BC concept. The BC's equivalent supply pressure, mass flow and frequency can all be modified from the original oscillator simulation. In the present work, the mass flow and pressure have been adjusted by as much as $\sim$18%, by scaling the density and pressure, while preserving the temperature, velocity and Mach number of the flow. The dominant jet frequence was set to $220Hz$, which was the frequency observed in the oscillator simulation when the full-tail simulations were started. The details of BC scaling have not been studied here. If sweep jets mature into a useful flow-control device, study of this topic is warranted.

The data in Fig. 10 are read and processed by a newly-developed Overflow BC subroutine. The subroutine reads the boundary-condition file once at the start of a run, and receives three input parameters during the course of a run: the "physical" time, the physical time-period (inverse frequency) over which to replay the boundary-condition file, and a phase shift. This is sufficient information to determine the correct time-plane in the boundary-condition data set, which is extracted using third-order Lagrange interpolation in the time-direction. The solution data are imposed at the boundary grid points without consideration of the mathematical characteristic of inflow and outflow. This is reasonable for choked flow, but not for lower-speed flows. Based on discussions with personnel involved with the full-tail testing, the phase of each of the 31 jets was set randomly. The frequency was set to be similar in all jets, so there is no "beats" phenomenon, in which jets move slowly through differing phase relations producing a low frequency signal envelope. A subtlety related to Overflow is that the nozzle throat grid on which the boundary conditions were applied was made small enough that Overflow's process of grid-splitting for load-balancing left this grid whole; this enabled simple programming of the boundary condition software.

Two validation tests were applied to the nozzle-throat BCs. Early in the work, the basic concept was tested. Two RANS simulations of a single jet were compared: one included the full interior and exterior flow, and the other was just the external flow, powered by the BCs. The processing needed to obtain a smoothly periodic solution was performed, but the jet pressure and mass flow were not altered in this test. Fig. 11 gives an overlay of contours of the streamwise momentum, and good agreement between the the two sets of contours is seen. (The jet operating conditions in this test differ from those used in the $38psig$ FML test, and thus the jet flow fields also differ.) Another validation test is to observe the history of the nozzle's vertical momentum flux coefficient CZ, in a full-tail simulation, given in Fig. 12. The installed jets oscillate principally in the x-z plane, and the CZ indicates the jets' flow angles. The CZ data are products of Overflow's loads integration routines, and they reflects what the CFD simulation is actually experiencing. CZ is a load applied to the body, so these momentum fluxes indicate fluctuating lift on the tail. The period of the signals matches that which was requested, $220Hz^{-1}$. The relative phase differences between signals are not regular, consistent with the input specification of random phases. The exact periodicity observed over two cycles is also as intended. Thus, the boundary condition process is functioning as intended; the external jet created by the boundary conditions is similar to the full interior-exterior simulation, and the integrated momentum fluxes have the appropriate frequency and phase.

VI. Full Tail with 31 Sweep-Jets

A primary goal of the Program's full-tail experiment was to demonstrate that the target for improved maximum loading on the tail can be achieved, and hence that sweep-jets are an effective flow control technology to retard boundary layer separation, at flight conditions. The goal of the CFD work is principally to replicate the experimentally observed aerodynamics. Because this flow is aerodynamically complicated, achieving

good agreement with experiment is viewed as a significant challenge. CFD also has the ability to provide a detailed picture of the fluid dynamics of the sweep jets. The primary challenges in the full-tail CFD simulations are the: (1) size and complexity of the grid system, (2) boundary conditions that provide the sweep jets, described above, (3) large ratio of time scale, from the time step needed to resolve the sweep jets to the overall time needed for flow convergence, and (4) turbulence modeling for the sweep jets.

VI.A. Geometry & Grids

The experimental test article is a Boeing 757 tail, obtained from an Arizona aircraft boneyard, and modified to include sweep jets. The 37 sweep jet oscillators and nozzles are in a housing strip that is roughly $1/2''$ thick, installed just upstream of the rudder hinge line on the starboard only side of the tail. The housing strip alters the native Boeing tail's shape and its aerodynamics, and its effect on the surface pressure is discussed below. The tail is mounted on a teardrop-shaped blister which is attached to the floor of the Air Force NFAC $40' \times 80'$ wind tunnel at NASA Ames Research Center. The blister elevates the tail out of the tunnel-floor boundary layer. Figure 13 shows the tail installed in the tunnel. The experiment is described in the papers by Andino[2] and Whalen.[20] The experiment measured distributed pressures and integrated loads on the tail over a wide range of operating conditions. The performance was observed to be very good at several operating conditions, including one with only the bottom 31 jets blowing, of the 37 installed. This case was selected for CFD simulations. The simulations have the lowest 31 jets blowing. All nozzles are present in the grid, but the top 6 jets have a no-flow-through boundary condition at the throat.

Several details are relevant to the comparison of experiment and CFD. For example, tail is $\sim 75\%$ of the height of the $40' \times 80'$ wind tunnel, and significant tunnel interference effects are expected. The wind tunnel walls are included in the simulations, but their geometry was not exactly preserved. The entire tunnel was approximated as having a constant cross-sectional area. The walls used in lieu of the tunnel's inflow bell-mouth and outflow diffuser are treated as slip walls. The starting point of the no-slip wall was adjusted to match the measured[12] boundary layer thickness of $\delta_{99} \simeq 12''$ in an empty tunnel, a short distance ahead of the tail's location. To account for the acceleration due to boundary layer growth in the test section, the normalized pressure and loads coefficients were computed using the estimated static and dynamic pressures at model location, excluding the model's effects. This is an approximation, as it neglects some additional change in the "local freestream" due to the tail's blockage effects. The wind tunnel walls diverge to accomodate normal bouhndary layer growth, and data are also corrected with the goal of minimizing tunnel effects in the data. The tail is old flight hardware.

The tail's interior is vented to the mounting blister interior, which then vents to both the tunnel interior and to atmospheric pressure surrounding the test section. "Bruch seals" are used to limit flow through the junctions between the tail, blister and tunnel floor. Pressures on the tail's interior surfaces contribute to integrated loads. The interior pressure is estimated as the average pressure around the perimeter of the tail-blister junction, and then applied to the tail-root area and included in CFD loads calculation. The interior pressure should principally affect the lift and drag, but not the side force. The experimental and CFD drag forces on the tail also includes the sweep jet thrust, and is reported as negative at some experimental operating conditions. The experimental data tables suggest that the uncertainty in yaw is $\beta \pm 0.5°$, and the uncertainty in the rudder angle is $< 0.01°$. CFD runs were at nominal values, $\beta = 0°, 5°$, not at the actual values. The rudder leading edge has "cut-outs" to provide hinge clearance at high rudder deflection; the cut-outs were covered with tape in some runs, and left open in others. The CFD geometry modeled neither the rudder mechnism nor the cutouts, and comparisons are with test data with covered cutouts.

The CFD grid system used in this work represents a balance between finite computational resources and the need for good spatial resolution of important flow features. The largest full-tail grid system has 575 individual block grids, with 518 grids devoted to the 37 jet nozzles, and 216M total grid points. The rudder deflection affects grid overlapping and overset connectivity, and a few extra grids were needed at the highest rudder deflection, $\delta_r = 30°$. The primary region of interest is downstream of the sweep-jet nozzles and on the rudder, but other regions must be resolved well-enough to enable a clear assessment of the sweep-jet simulation. Figure 14 gives an image of the surface grid, decimated by 2 in both surface coordinate directions. An "intermediate-field" grid was designed to cover the sweep jets through an expected region of strong adverse pressure gradient on the forward part of the rudder, and it appears as a dark band downstream

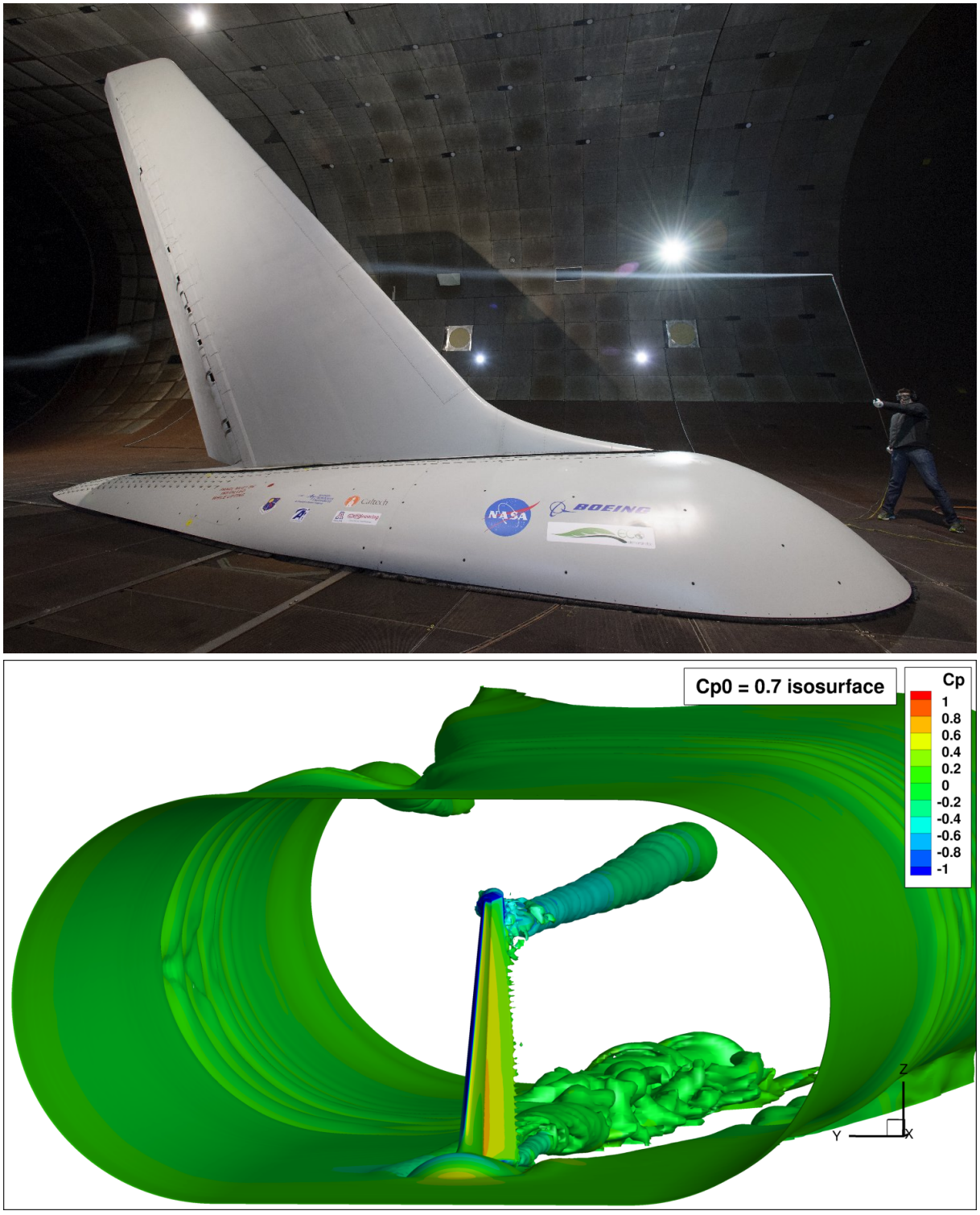

Figure 13: Full tail installed in NFAC $40' \times 80'$ wind tunnel. Smoke flow-visualization testing (top). CFD isosurface (bottom) of stagnation pressure coefficient, $Cp_0 = 0.7$, colored by Cp. Key features that are visible include: The tail with a deflected rudder on its mounting blister; Tail tip, rudder root, and blister horseshoe vortices; Agglomeration of tunnel boundary layer fluid due to tail-induced circulation; Small short "streamers" on the rudder trailing edge from non-uniform boundary layer thickness on rudder with active sweep jets, flowing off rudder and into wake.

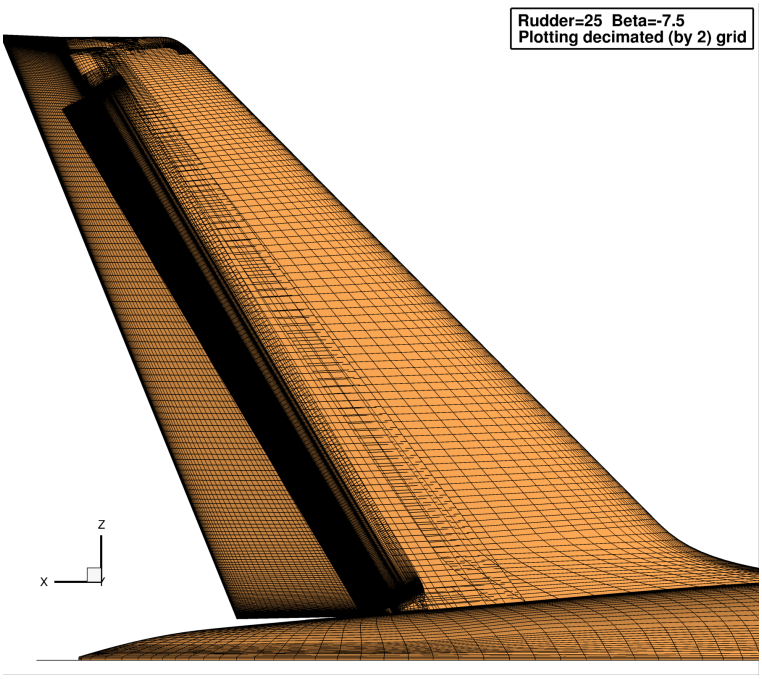

Figure 14: Surface grid on the tail, showing every second grid line. The dark band on the front section of the rudder is the intermediate-field grid, intended to resolve the near- to intermediate-field of the sweep jets.

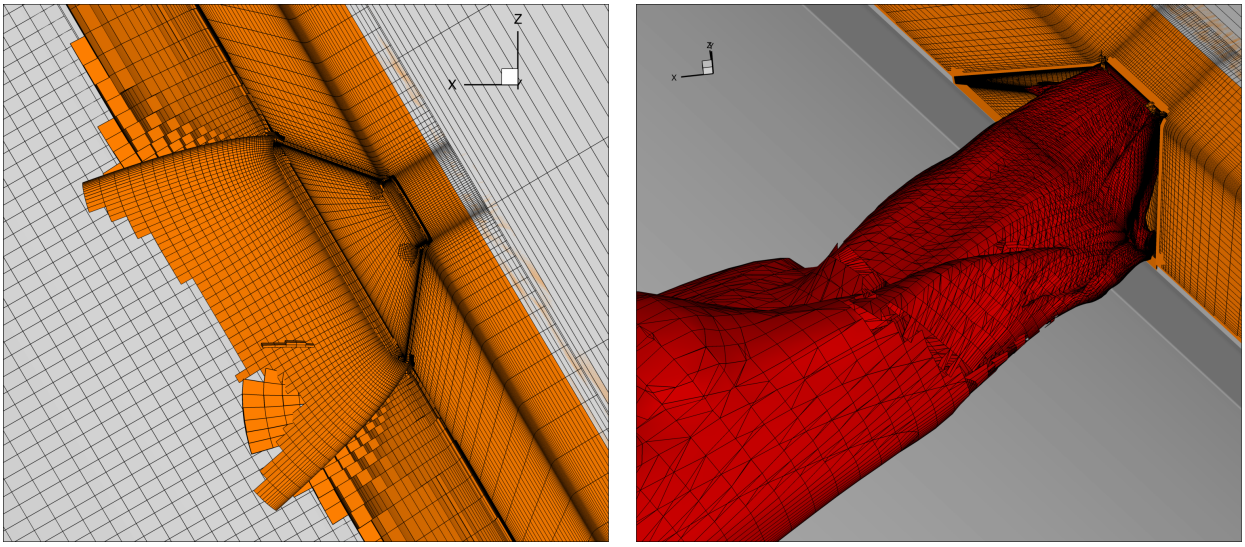

Figure 15: Grid for a single sweep-jet nozzle (left) with the 14 grids associated with each nozzle highlighted in orange. A $M = 0.4$ isosurface of sweep jet highlighted in red (right), with full-resolution grid spacing.

of the rudder hinge line. The sweep jets oscillate in the vertical direction, and they can be can be anywhere on the rudder, instantaneously. The intermediate-field grid spacing is uniform at $\Delta\zeta = 0.1''$ where ζ is "up" the rudder; this grid has $3045 \times 71 \times 96$ points in the directions up the rudder, quasi-streamwise, and normal to the wall. The rudder grid aft of the intermediate-field grid was not highly refined, as part of the compromise between computational cost and accuracy.

It is essential to recognize what grid spacing is achieved on flow features relevant to sweep jet performance. The grid resolution of the near-field jet is shown in Fig. 15. The grids highlighted in orange are associated with each nozzle, and are repeated at all 37 nozzles. The grey grids are associated with the tail and rudder as a whole; for example, the intermediate-field grid is seen in the left side of the left image. Only the active grid points, as selected by the Pegasus overset grid-connectivity software, are show (although the plotting routine

is not fully precise in rendering this distinction.) The nozzle throat has 69×91 grid points, in contrast to the 201×291 grid points at the nozzle throat used for the single sweep-jet simulations. The grids lines overlayed on the $M = 0.4$ Mach number isosurface of a sweep jet, in the right image, is a straightforward and relatively meaningful image of grid resolution. Counting grid lines (and we rotated the image to see the full jet) reveals that the near-field grids have ~ 25 grid points across the width of the jet, and the intermediate-field grid has ~ 16 points across the vertical dimension of the jet at this location. The choice of the $M = 0.4$ isosurface is somewhat arbitrary, but reasonable; it slightly exceeds the local Mach number of the non-jet flow at $M \sim 0.3$, and thus is close to what we think of as the "outer edge" of the jet.

A critical assessment of the current grid resolution must conclude that some regions of the flow are significantly under-resolved. The ~ 16 grid points across the jet, in combination with the fifth-order spatial discretization, is probably "borderline adequate" to provide weak algorithmic diffusion in the momentum convective terms, if the jet had a smooth fully-developed velocity profile. However, as seen in the single-jet results in Fig.6, the near-field jet has a potential core surrounded by a shear layer; that shear layer cannot be well resolved on this grid. Even less well resolved are the turbulence variables of turbulence model with transport equations. Turbulence variable have peak near the middle of a simple shear layer, so they require roughly half the grid spacing that is needed to resolve the Navier-Stokes variables in a shear layer. This simulation is very likely affected by cancellation of errors in some regions: the modeled turbulence is under-resolved and therefore artificially weak, but these effects are partially offset by moderate algorithmic diffusion of the jet's resolved momentum field.

VI.B. Simulation & Processing Details

Details of how the full-tail simulations were run and processed are summarized here. The full-tail sweep-jet simulations were run using a "bootstrap" strategy that involved starting from initial conditions that were close to the final state. In LES, the computational cost scales linearly on the ratio of convergence time to time step. Thus, reducing the physical time needed to converge the flow is one means of reducing CPU costs. The total physical time needed for a flow to reach its asymptotic state cannot be accurately anticipated in most cases, but the convection of loads-induced circulation sets a lower limit on that time. The starting solutions were obtained using steady jets, in lieu of the unsteady sweep jets, run with the same mean mass flux as the sweep jets. Steady jet cases achieved side-force coefficients that were often only a few percent below the sweep-jet results, but they could be run at time steps which were $O(100)$ times larger than the LES time step and would converge in $O(10^3)$ time steps. When the sweep-jets were then "switched on," the steady jet flow field is replaced by the sweep-jet field in some small multiple of the flow-through time period, for flow over the rudder. Convergence after starting the sweep jets involves, in these cases, a relatively small change in the global circulation field, and convergence to some tolerance is faster than starting the sweep-jet simulation from crude initial conditions. There are potential deficiencies in this bootstrap approach, for example, adverse effects of hysteresis and non-uniqueness, and the probability that the strategy for setting initial conditions yields a poor approximation of the final state, at some operating conditions.

An example of a simulation, run as described above and with DDES turbulence modeling, is presented in the history of the side force coefficient CY in Fig.16. This history starts at iteration $iter \sim 1500$, after the steady-jet steady-state RANS simulation was almost converged. The side force CY without tunnel corrections starts at $\sim 97\%$ of its asymptotic value of $Cy \sim 1.27$. The rudder flow-through time period is roughly $0.05s$, and much of the increment in rudder side force becomes established in $0.1s$, after switching to sweep-jet boundary conditions. This simulation appears poised to move to a slightly higher CY, were the simulation to be continued. Typical of our general experience in D/DES simulations, some degree of convergence uncertainty must be accepted in the results, so this uncorrected load is $CY = 1.27 \pm 0.004$. The averaged integrated loads displayed in subsequent figures are obtained from long-time averages, which in this case was from $iter = 27k$ to the end. Loads are then corrected for the freestream at the tail's location. This simulation was run for 894 hours on 800 Ivy Bridge cores for a total of $\sim 715k$ CPU-hours.

The time step used to compute the oscillator flow, $5\mu s$, is smaller than needed for the full-tail simulation which uses coarser grid spacing and cannot resolve such small length and time scales. The time step was set to $25\mu s$, and the effects of time step on accuracy were not evaluated.

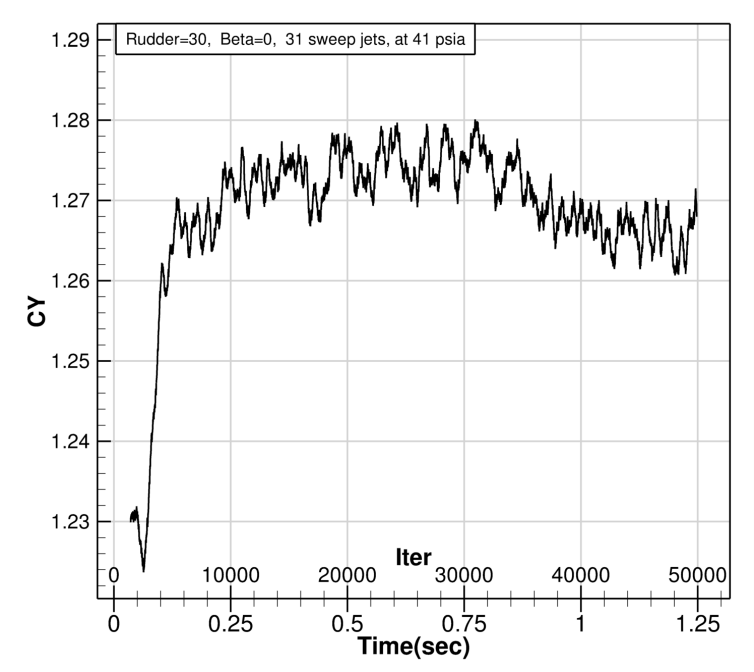

Figure 16: History of the native Overflow load history, at total mass-flux of $2.94 lbm/s$, after restarting from a solution run with steady jets in lieu of sweep jets.

Data were recorded during the simulation to provide accurate mean and fluctuation data from the simulation results. The flows were simulated over many PBS job submissions. For each PBS job, Overflow was directed to accumulate the running time average and some unsteady statistics, over just that PBS job. The complete instantaneous loads history is also recorded. When the loads were adequately converged, over a sufficient time, the appropriate short-time averages were then combined to give a single set of mean and fluctuation results, representative of the asymptotic unsteady solution.

VI.C. Mean-Flow Simulation Results

CFD results are presented for several simulations of the Boeing 757 tail, with and without sweep-jets powered in the lowest 31 of the installed 37 nozzles. All results presented are for a nominal yaw angle of $\beta = 0$. Figure 17 shows that the flow is fully separated at the top 6 sweep-jet nozzles which are unpowered, and it is attached at all lower sweep jets which are powered. There are also pockets of low-speed flow near the trailing edge, and between the jets in the upper-most 7 of the powered jets, which may indicate local incipient separation. Near the base of the tail, the rudder's streamwise length is $l \sim 80''$ compared to the jet's initial dimensions of $0.5'' \times 0.25''$, for a geometric mean dimension of $d = 0.35$. Thus, the sweep jet's influence in the boundary layer persists to $l/d > 200$.

Figure 18 gives the three most important integrated loads: side force, drag, and yawing moment about the quarter chord, in the body axis, denoted $CYBA$ $CDBA$ and $CNBA25$. These plots include experimental results at four power settings as characterized by the differential pressure, *psid*, between the sweep-jet supply and ambient: off, $7.5psid$, $27psid$ and $33psid$. The experimental data points are at $\delta_r = 0°, 15°, 20°, 25°$ and $30°$. The jets-off data exhibits the onset of stall as the rudder angle δ_r increases to $30°$. Increasing the jet's supply pressure from $\sim 0psid$ to $7.5psid$ and $27psid$ gives a montonic increase in the magnitude of $CYBA$ and $CNBA25$ across all δ_r; the further increase to $33psid$ gives a small further increase except at $\delta_r = 25°$.

The CFD results are in close agreement with the appropriate experimental data. CFD simulations were run with $27psid$ and $38psid$ sweep jets. The $38psid$ sweep jet boundary conditions are from the single-jet simulation, and unscaled; the $27psid$ BCs are the $38psid$ BCs with pressure and density scaled down to the lower supply pressure. Results for SST RANS and DDES turbulence modeling are included, but little

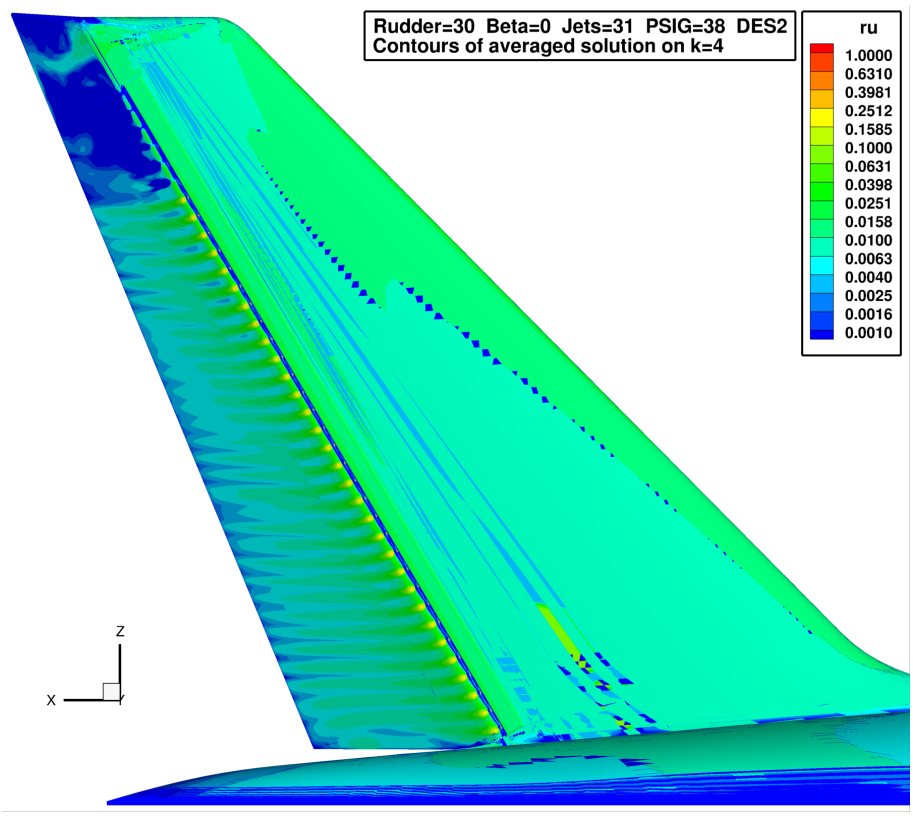

Figure 17: Time-averaged streamwise momentum (ρu) in the boundary layer just above the surface, from simulation using DDES turbulence modeling. Dark blue indicates reversed flow. The individual sweep jets are visible. Incipient flow reversal near the trailing edge of lower rudder, shown by thin blue wedges. Full separation on upper rudder, where the uppermost 6 sweep-jets are not powered. (The blue 'stripes' and 'diamonds' on the tail are IBLANK-related plotting anomalies.)

difference is seen between these models, in these results. For the jets-off results, the CFD side force is slightly higher than the measured load, with the difference increasing to ~ 0.04 at $\delta_r = 30°$. The drag and yawing moments are similar in the CFD and experiment. For powered sweep jets, the side force is slightly overpredicted, but by a smaller amount than seen in the jets-off cases. The predicted pitching moment agrees well with experiment at all conditions. The tail's drag coefficient was natively computed (by Overflow) by integrating the tail's exposed surfaces, but excluding the area of the sweep-jet nozzle. The experimental loads are from a balance, and it includes the sweep-jet thrust. Thus, the simulation's aggregate nozzle momentum flux CX is included in the drag results plotted here, to achieve similarity between experiment and CFD. The jet thrust contribution added to CDBA is -0.0062 at $27psid$ and -0.008 at $38psid$.

The surface pressure coefficient Cp results are given in Figs. 19 and 20. The first of these Figures illustrates the pressure tap locations, which are arrayed along horizontal and quasi-vertical lines. The lowest three of the horizontal lines, at fixed vertical heights, VA, VB and VC, are within the lowest 31 sweep jets which are powered, at this operating condition; the top row, VD, is within the top 6 jet nozzles that are unpowered. The flow conditions for the results given in Fig. 20 are $\beta = 0$, jet supply pressure $41psid$ and rudder delection $\delta_r = 30°$. Results for DDES and RANS turbulence modeling are given.

Several features of the Cp distributions are noted. The flow is from left to right, and the sweep jets affect the suction side of the rudder, which is the upper curve on the right side of each plot. There are typically four suction spikes on the suction side: (1) the tail's leading edge, the (2) leading and then (3) trailing corners on the housing which encloses the sweep-jet oscillators, and finally (4) the rudder's curved leading edge, over which the sweep jets flow. The rudder hinge line is close to the right-most of the suction spikes. On the pressure side of the tail, there is a broad pressure maximum at the rudder hinge line. A cluster of pressure taps reporting $Cp \sim -0.1$ near the rudder hinge line are within the cavity of the rudder hinge, and

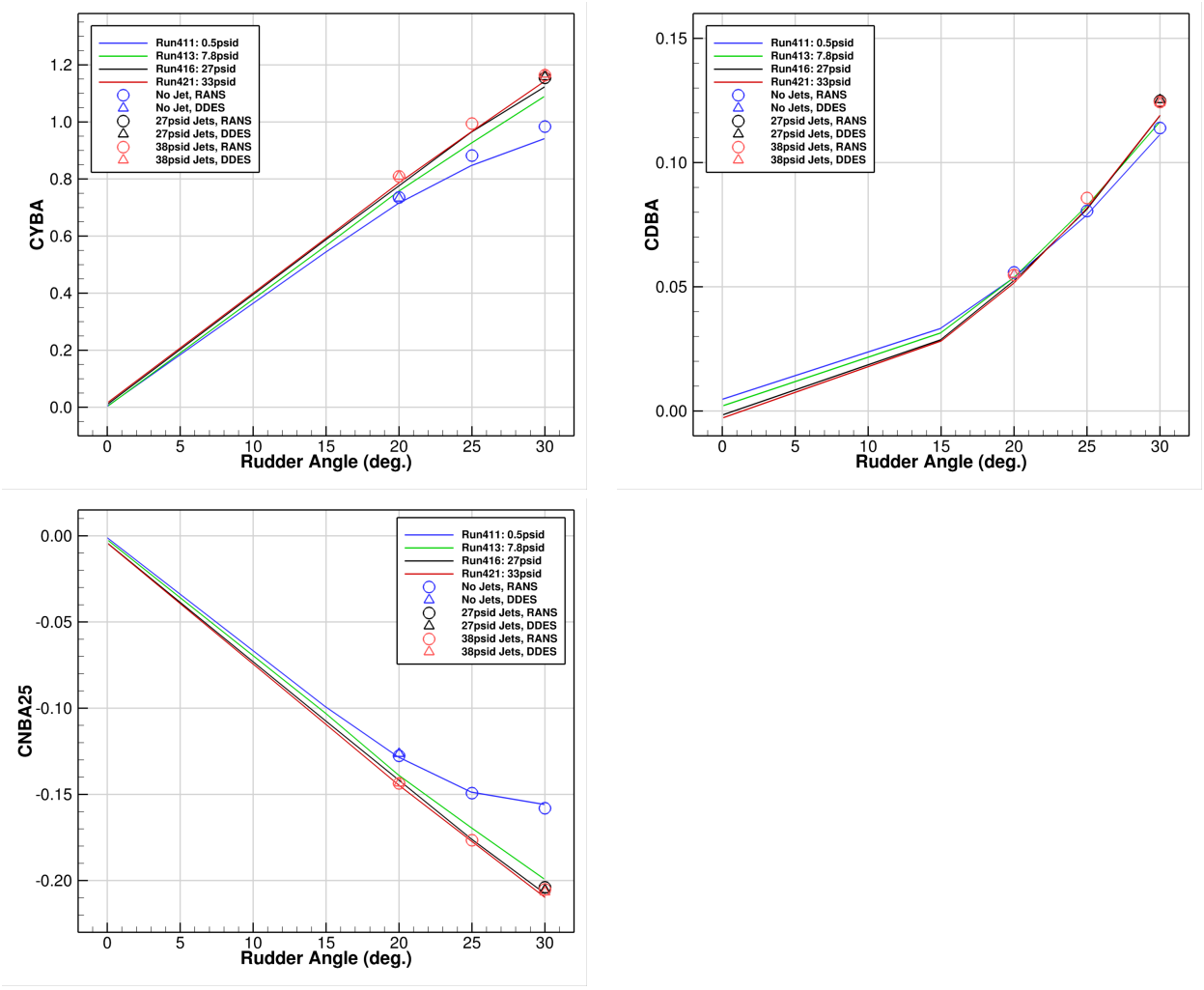

Figure 18: Time-averaged integrated load coefficients: side force, drag, and yawing moment as functions of rudder deflection angle. At operating conditions $M = 0.15$, $\beta = 0$. All CDBA data, experiment and CFD, include sweep-jet thrust.

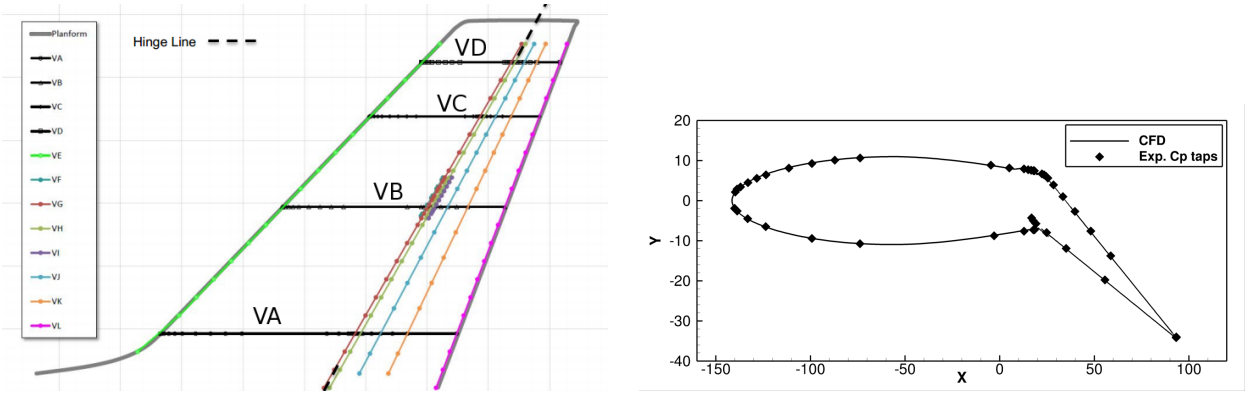

Figure 19: Pressure tap locations: the horizontal tap rows, the lowest VA to the highest VD. Individual pressure tap locations in the VA plane plotted with the CFD surface (not to scale). Note the interior taps, near $x = 20$, resulting from rudder deflection.

do not measure the exterior pressure. The RANS and DDES CFD results are very similar except for the top pressure row, VD, where the flow is separated.

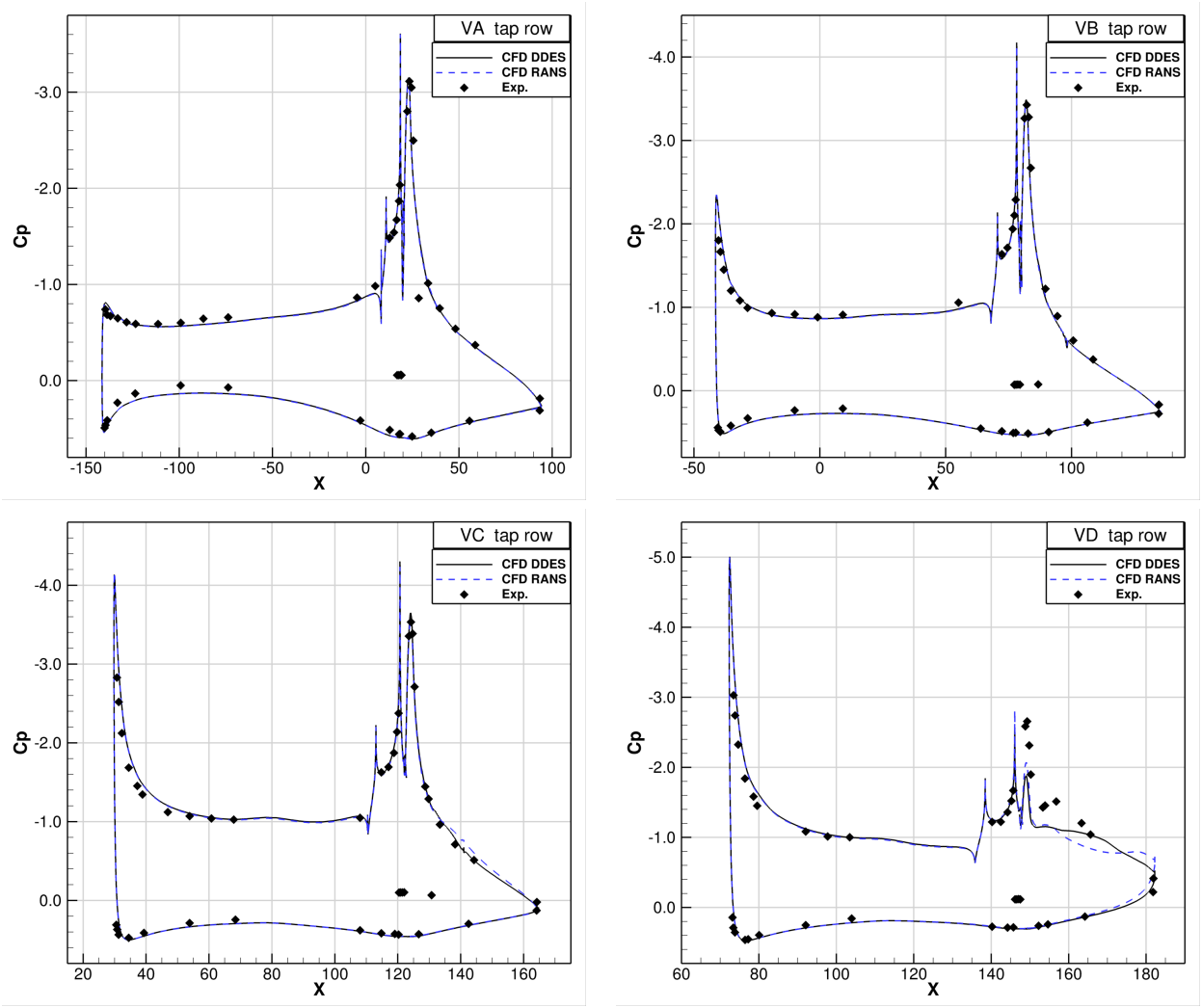

Figure 20: Surface pressure coefficient at the four horizontal (streamwize) tap rows: VA, VB, VC, VD. Operating at $M = 0.15$, $\beta = 0$, sweep jet supply pressure $41psid$, and rudder delection $\delta_r = 30°$. Results for SST RANS and DDES turbulence modeling.

The agreement between CFD and experiment pressure distributions is excellent at most locations within the lowest three measurement stations, VA - VC, where the sweep jets are powered. On the rudder, the difference between experiment and CFD is consistently $\Delta Cp < 0.1$ and typically even smaller. The largest discrepancies in Cp are seen on the pressure side of the fixed tail at the VA station and on the suction side side of the fixed tail at the VB and VC stations. This pattern of discrepancies with experiment is frustrating; the largest differences occur in regions that ought to be simulated well by a Navier-Stokes solver. The discrepancy here implies that some "global" difference in between experiment and CFD must exist, and then, that the minimum uncertainty in the Cp is larger than the observed discrepancy on the rudder. The apparent high accuracy in predicted Cp on the rudder should be viewed as somewhat fortuitous.

The largest differences between CFD and experiment *Cp's* occur in the separated flow at the VD station, where the sweep jets are not powered, and where the flow is separated. Ironically, in this simulation, separated flow is a greater challenge to accuracy than the sweep jets.

The differences between RANS and DDES results are negligible at the VA and VB stations, and only become visible at the VC and VD stations. This result must be interpreted cautiously. The streamwise grid spacing dominates the DDES switching between RANS and LES modes, and that grid spacing decreases with increasing height, as seen in Fig. 14. Thus, the DDES model has a greater tendency to operate in its RANS mode on the lower part of the tail, and in its LES-mode on the upper tail. The apparent subtle

superiority of the DDES result at the VC station is probably not a significant indicator of accuracy, given the discrepancies in Cp elsewhere. At the VD station, neither RANS or DDES simulations match the suction spike on the leading edge of the rudder, nor downstream to roughly the middle of the rudder, at $x \sim 170$. The grid is designed to capture the sweep jets, and it may not be as good as needed to resolve the native jets-off turbulence in a separating flow over the rudder hinge and sweep-jet housing.

VI.D. Simulated Sweep-Jet Dynamic Structure

The preceeding results demonstrate that these simulations can replicate the averaged behavior of the sweep jets, at these conditions, with good accuracy. This does not imply that jets' dynamics are captured well. Nor are there experimental measurements for this operating condition that will permit an evaluation of the simulated sweep-jet dynamics. This section, therefore, examines the sweep jet structure, with the goal of providing insights into dynamical simulation accuracy and the turbulence physics of the flow.

To enhance the ability to visualize the flow, a simulation was run with two gas "species," both of which are air. The gas from the sweep-jet nozzles is the second specie, which is then used to track the trajectory of the jet fluid. This simulation is at the same condition as above: $\beta = 0$, $\delta_r = 30°$ with $27psid$ sweep jets, and run with DDES modeling; the two cases should by aerodynamically identical. Three quantities are used to generate 3D isosurfaces, in an effort to visualize the structure: jet specie (4% concentration), local streamwise vorticity ($\omega_i u_i/|u| = 0.004$), and stagnation pressure coefficient $Cp_0 = 0.7$, shown previously in Fig. 13.

The simplest conceptualization of the jets' dynamical structure is sinuous trail of jet fluid, imposed on the mean streamwise vorticity created by the average $-z$ component of the jets' thrust, which itself exists in the mean 3D flow on the rudder and its adverse pressure gradient of the rudder. With a frequency of $220Hz$, and an boundary-layer edge Mach number averaged over the rudder of $M \sim 0.2$, the flow should produce a sinuous jet wavelength of roughly $\lambda \sim 12''$. If each period of the wavelength rolls-up into some vortex structure, there should be roughly 7 such structures in the streawise distance from sweep jet nozzle to the end of the rudder, in the $\sim 80''$ rudder chord near the root of the rudder.

Figure 21 give specie and streamwise vorticity isosurfaces. Specie and streamwise vorticity isosurfaces tend to show that structures form in the near-field, within 1 jet wavelength λ of the nozzle, which then convect downstream while preserving essential features of that structure. The jet specie tends to follow a divided path; some of it flows essentially along the mean streamlines near the rudder surface (as inferred from Fig. 17), while the outer jet tends to clump into "puffs" of jet fluid that slowly flow root-ward relative to the near-wall jet fluid. Near the root, 7 such puffs along each jet trajectory are visible, while $3 \sim 4$ puffs are seen closer to the tip. The vorticity isosurface show clumps with more complicated structure than seen in the jet specie, and in some regions the clumps tend to merge into short bands that span a few vertically adjacent jets. An alternate description of that phenomenon is that short-range phase-coherent arrays appear in the structure, as if there is a "preferred" arangement of the structures in adjacent jets. However, the initial sweep jets have random phase, so the lattice is not coherent over large areas. Figure 22 shows the streamwise vorticity pattern near the root, at four times over a jet oscillation period. The most dominant structure to the lead author's eyes is an elongated right-handed spiral centered on the streamwise direction. This spiral has an outer-layer structures of streamwise vorticity, with a WNW-ESE orientation, and an inner-layer structure with NE-SW orientation. This, however, is a subjective observation.

Turbulent shear stress and the ability to resist separation result when the sweep-jet vortical structure induces an exchange between the higher-speed outer flow and the lower-speed near-wall flow. An isosurface of stagnation pressure is a good means of discriminating between these high- and low-speed regions, especially in the presence of a mean streamwise pressure gradient. Figure 23 shows isosurfaces of the stagnation pressure coefficient $Cp_0 = 0.7$ ($Cp_0 = 1.11$ in the freestream, uncorrected for tunnel acceleration effects) and streamwise vorticity. The viewpoint is downstream of the rudder, to help visualize the height of the Cp_0, and $+z$ is to left of the images. Several features in these images are noted. Near the leading edge of the rudder, where the solution is run on the relatively fine near-field and intermediate-field grids, there are small loops in Cp_0which are vortices on the sweep jets. The loops are best seen in the left images, while the right images show that the loops commonly encompass regions of streamwise vorticity. This structure is broadly consistent with turbulent vortices forming on individual and independent jets. The fine-scale turbulence on the finer

grids near the nozzles is lost when the flow passes onto the main rudder grid (the lower $\sim 75\%$ of the visible rudder). Again, the streamwise vorticity seems to align in locally phase-coherent arrays, but the structures appear as loops, many of which have a similar orientation, from this viewpoint. The $Cp_0 = 0.7$ isosurface displays a dominant streamwise structure, which is presumably due to the mean streamwise vorticity of the

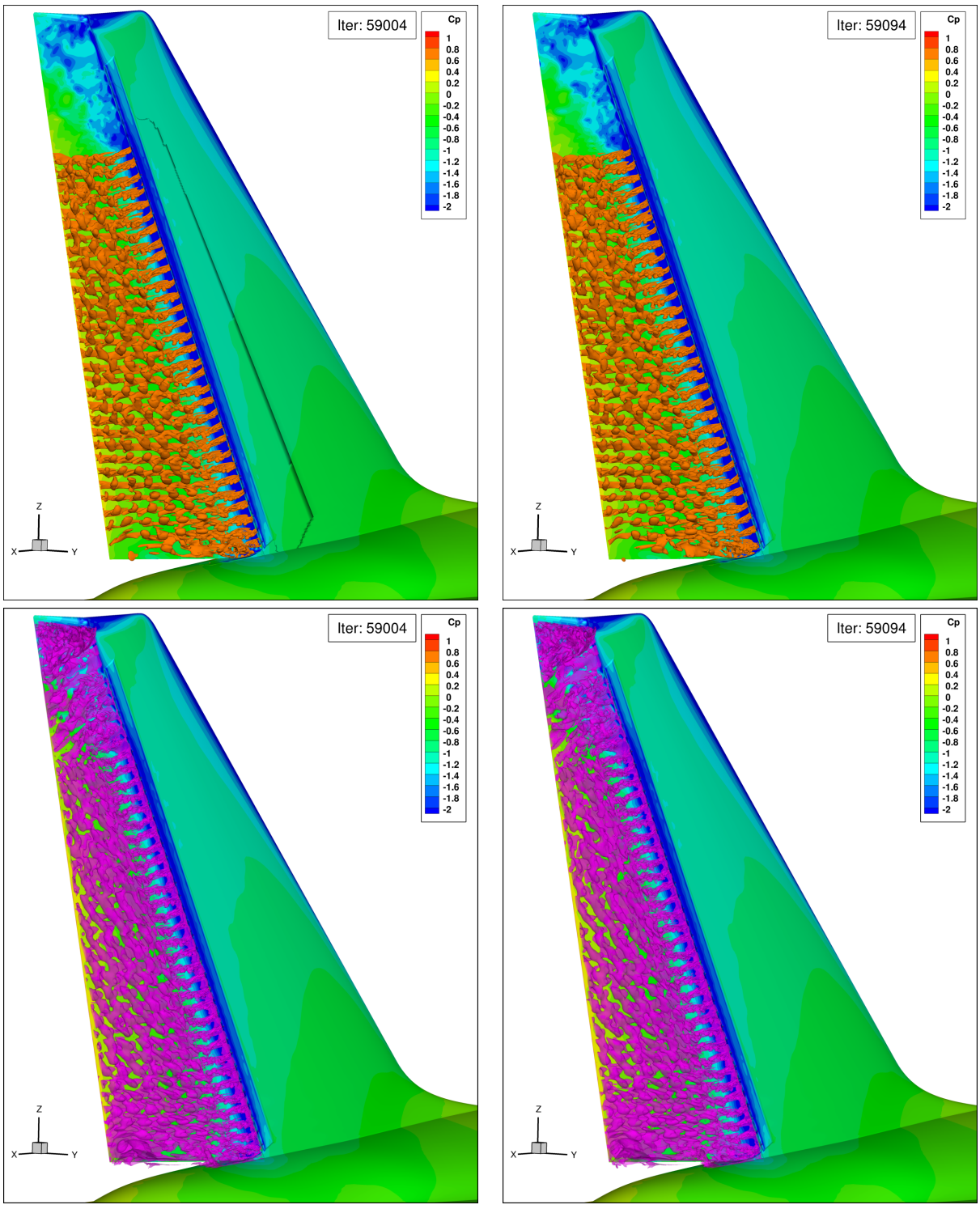

Figure 21: Isosurface of jet "specie" concentration (orange, upper images) and local streamwise vorticity (violet, lower images) at two times separated by half a sweep-jet period, $2.3ms$. Contours of Cp are given on tail and rudder surface. DDES simulation at $\beta = 0$, rudder deflection $\delta_r = 30^\circ$ and with $27psid$ sweep jets.

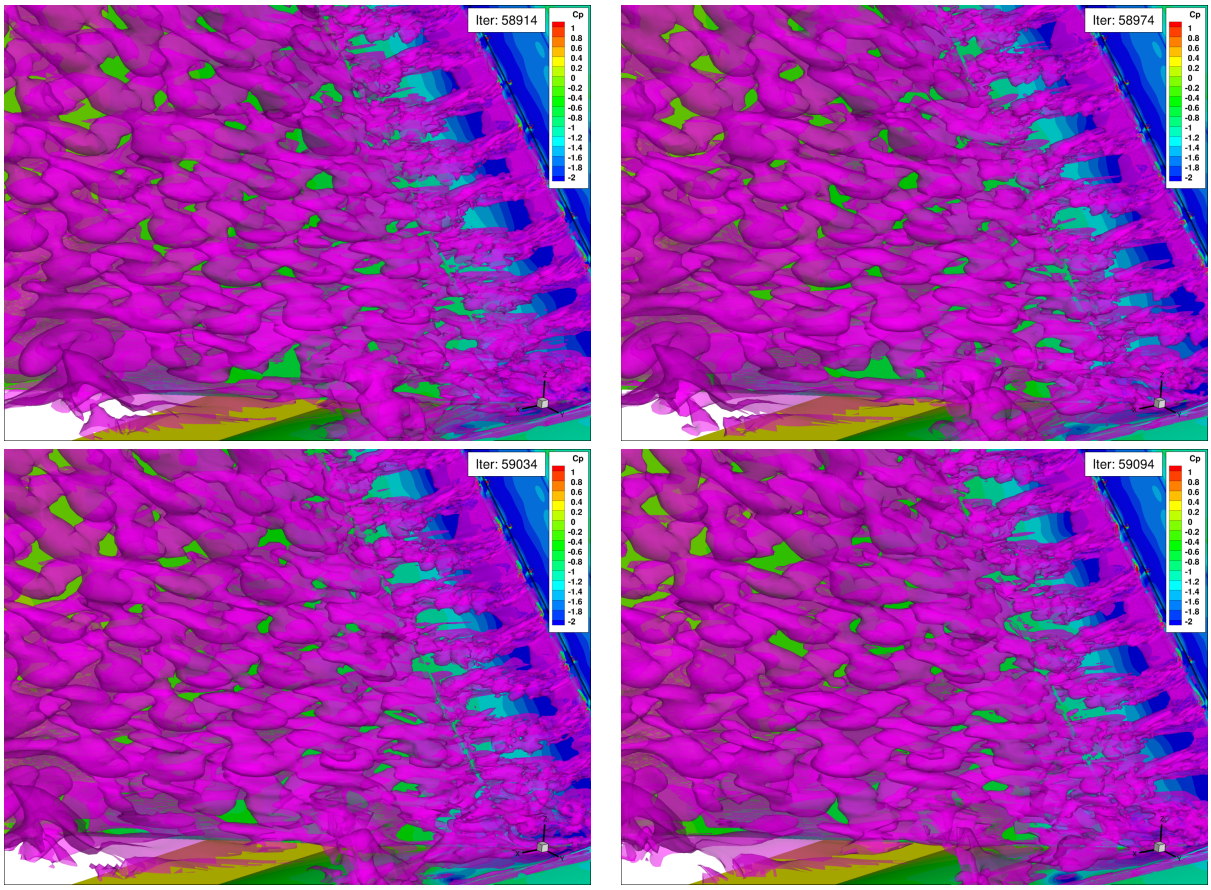

Figure 22: Isosurface local streamwise vorticity, near the rudder root, at four times over one sweep-jet period. Contours of Cp are given on tail surface.

jets. There are also relatively periodic streamwise variations on the height of the $Cp_0 = 0.7$ layer which are associated with the dynamic structure in the streamwise vorticity. This streamwise variation in the $Cp_0 = 0.7$ height provides a means for the the dynamical structure of the outer flow to transfer energy to the inner flow, which would contribute to suppressing boundary layer separation.

The implications of these images of the dynamical structure are uncertain, at present. There is clearly a significant loss in the resolved turbulence between the finer near-nozzle grids and the downstream main rudder grid. This loss certainly degrades the accuracy of the simulation, but we cannot know if the essential features of turbulence that suppresse boundary layer separation are well represented in the simulation. Because the mean surface pressure distribution matches the experiment, we can only reliably state: the simulation is not obviously inaccurate in a gross sense. Ironically, this loss of detail turbulence probably helps provides a clearer view of the turbulent structures, as those structures are hard to view when there is a wide range of turbulent scale. In retrospect, the relatively fine intermediate-field grid should be extended to the trailing edge of the rudder. The CPU cost increase will be $O(10\%)$ of the total cost, and it would significantly reduce the likely uncertinty in the results.

VII. Summary & Conclusions

The goal of the present work is to demonstrate the ability of CFD to simulate sweep-jet active flow control devices, which are used to suppress boundary layer separation and hence improve aerodynamic performance. The present application is a Boeing 757 vertical tail, modified to include an array of 38 sweep jets just upstream of the rudder hinge-line. However, practical and effective flow control may be useful in myriad applications. This effort is one element of NASA's Environmentally Responsible Aviation (ERA) program, whose goal is to explore technologies that reduce the adverse environmental effects of aviation.

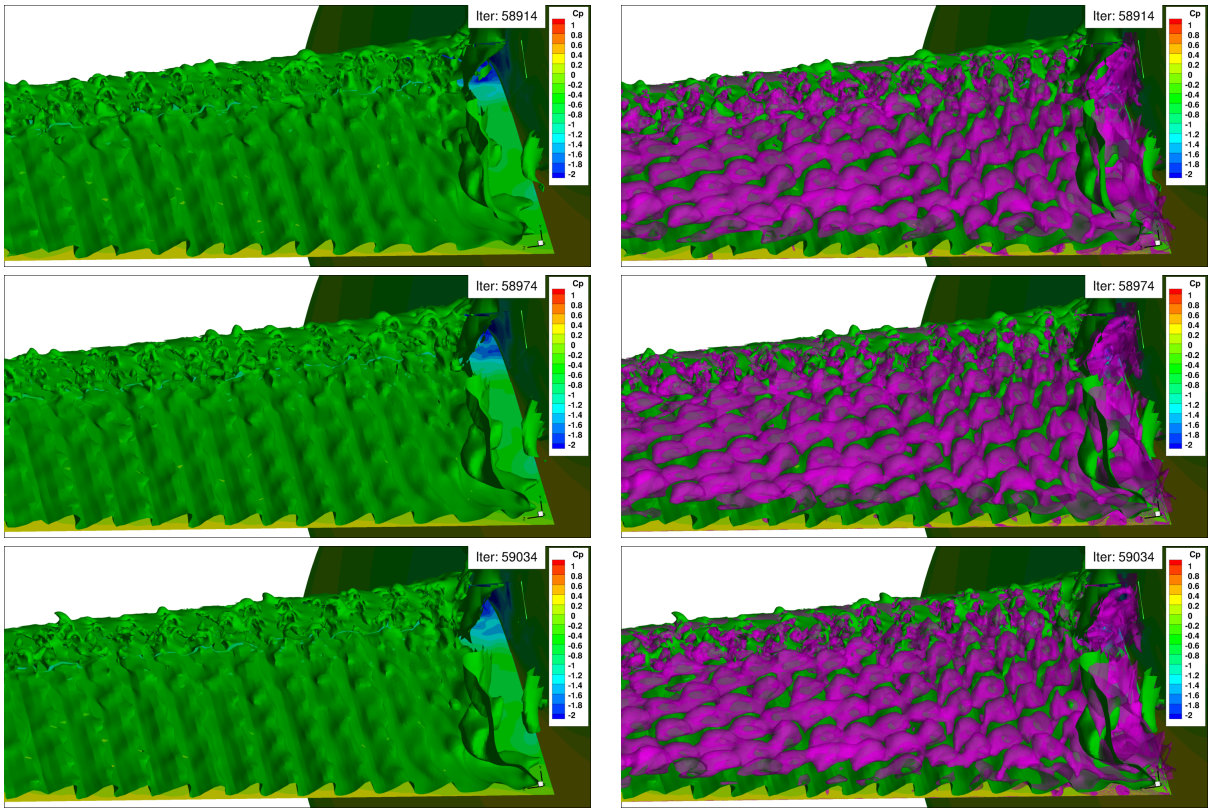

Figure 23: Isosurface $Cp_0 = 0.99$ (green) and local streamwise vorticity (violet). left frames show just $Cp_0$to illustrate the structure of lower-speed flow, and right frames show Cp_0overlayed by streamwise vorticity.

The focus of the simulation work is a Boeing 757 tail, augmented with sweep-jet flow control ahead of the rudder hinge line that delays the onset of stall to higher rudder delection, relative to a conventional tail. The simulation is developed in steps: first simulations were performed on a single fluidic oscillator and its sweep jet, then the sweep-jet boundary conditions derived from the single jet simulation, and finally the full tail with many sweep jets. This strategy reduces the considerable computational cost, relative to simultaneously simulating 31 fluidic oscillators and sweep jets and the full exterior flow field, by an order of magnitude.

Simulations were performed with Overflow, using a fifth-order spatial algorithm for convective terms, which is certainly critical to computational efficiency and simulation accuracy. Grid refinement was based on aerodynamics experience; *ex post facto* engineering judgement identifies regions where further grid refinement is probably needed. The turbulence models considered included the SST-RANS, SSTDES and SST-DDES models. The SST-RANS model performed best in the oscillator interior, and SST-DDES is preferred for the external flow, although we have limited ability to discriminate between it and SST-RANS.

The accuracy of the simulations appears to be very good, but these are complex flows and the ability to predict the full range of flow control effectiveness is unknown. For the oscillator interior flow, the measured and simulated dominant oscillator frequencies agree very well, but the frequency resolution in the simulation is only $\sim 7Hz$, due to the limited duration of that simulation. The peak-to-peak magnitude of the simulated pressure signal is about 75% of the measured value. DES turbulence modeling was distinctly inferior to RANS modeling in predicting the oscillator interior flow.

Accuracy for the mean-flow behavior on the full Boeing 757 tail simulation is very good, at the conditions simulated. The integrated loads agree well with measurements at the high jet blowing rates which achieved the Program goal of good performance augmentation. The surface pressure distributions were also very good, especially on the suction surface of the rudder where the sweep jets were powered; the largest discrepancy with the measure surface pressures occurred in the separated flow where the sweep jets were unpowered. It is important to recognize that because the rudder boundary layer remains attached, at the flow conditions

studied, all simulations that achieve attached flow could give similarly good results. Simulations with the Euler-equation fall into this catagory. The real test of accuracy of these types of simulations will occur under a range of flow conditions that display varying levels of flow separation on the rudder.

The dynamical vortex structure induced by the sweep jets is a critical means of understanding and improving flow-control performance of the jets. We cannot here validate the accuracy of the predicted vortex structure, and so the present observations are not the final word on this topic. These structures are observed to be large enough that the eddies from neighboring jets interact strongly. Short-range order among the eddies was observed, in which, presumably, the neighboring eddies coexist without a rapid cascade of turbulence energy to heat. The ability to generate persistent structures that are also effective at mixing near-wall and outer-layer fluid is expected to be a key feature of successful flow control.

References

[1]http://www.aeronautics.nasa.gov/iasp/era/index.htm "NASA ERA Project"

[2]Andino, M.Y., Lin, John C., Washburn, A.E., Whalen, E.A., Graff, E., Wygnanski, I.J., "Flow Separation Control on a Full-Scale Vertical Tail Model using Sweeping Jet Actuators" AIAA 2015-0785

[3]Bres, G., Fares, E., Williams, D., and Colonius, T., "Numerical Simulations of the Transient Flow Response of a 3D, Low-Aspect-Ratio Wing to Pulsed Actuation," AIAA-2011-3440.

[4]DeSalvo, M., Whalen, E., and Glezer, A., "High-Lift Enhancement using Fluidic Actuation," AIAA-2010-0863.

[5]Gatski, T. and Rumsey, C., "CFD Validation of Synthetic Jets and Turbulent Separation Control," http://cfdval2004.larc.nasa.gov

[6]Gokoglu, S., Kuczmarski, M., Culley, D., and Raghu, S., "Numerical Studies of a Fluidic Diverter for Flow Control," AIAA-2009-4012.

[7]Gokoglu, S., Kuczmarski, M., Culley, D., and Raghu, S., "Numerical Studies of a Supersonic Fluidic Diverter Actuator for Flow Control," AIAA-2010-4415.

[8]Gokoglu, S., Kuczmarski, M., Culley, D., and Raghu, S., "Numerical Studies of an Array of Fluidic Diverter Actuators for Flow Control," AIAA Paper 2011-3100.

[9]Kushner, L.K., Heineck, J.T., Storms, B.L., and Childs, R.E., "Visualization of a Sweeping Jet by Laser Speckle Retro-reflective Background Oriented Schlieren," AIAA-2015-1697

[10]Menter, Florian R. "Improved two-equation k-omega turbulence models for aerodynamic flows." NASA STI/Recon Technical Report N 93 (1992): 22809.

[11]Menter, F. R., Kuntz, M., and Langtry, R., "Ten Years of Industrial Experience with the SST Turbulence Model," Turbulence, Heat and Mass Transfer 4, ed: K. Hanjalic, Y. Nagano, and M. Tummers, Begell House, Inc., 2003, pp. 625 - 632.

[12]Mort, Kenneth, W., "Boundary Layers and Wall Pressures in 40-by-80-Ft. Wind Tunnel with Deep Cavity Acoustic Lining" Prepared for NASA/Ames Research Center, BPA/54869D(MXD), Call No. 54, Aug. 28, 2000.

[13]Seele, R. Graff, E., Gharib, M., Taubert, L., Lin, John, and Wygnanski, I., "Improving Rudder Effectiveness with Sweeping Jet Actuators," AIAA 2012-3244

[14]Shmilovich, A., Yadlin, Y., and Whalen, E., "Computational Evaluation of Flow Control for Enhanced Control Authority of a Vertical Tail" AIAA-2015-3311

[15]Suhs, N. E. Rogers, S. E., and Dietz, W. E. "PEGASUS 5: An Automated Pre-processor for Overset-Grid CFD," AIAA Paper 2002-3186, AIAA Fluid Dynamics Conference, June 2002, St. Louis, MO.

[16]Tramel, R.W., Nichols R.H., and Buning P.G., "Addition of Improved Shock-Capturing Schemes to OVERFLOW 2.1" AIAA-2009-3988.

[17]Vatsa, V.N., Koklu, M., Wygnanski, I., Fares E., "Numerical Simulation of Fluidic Actuators for Flow Control Applications," AIAA-2012-3239.

[18]Vatsa, V.N., Casalino, D. Lin, J.C., Appelbaum, J., "Numerical Simulation of a High-Lift Configuration with Embedded Fluidic Actuators" AIAA-2014-2142.

[19]Whalen, E.A. and Goldhammer, M.I. "Active Flow Control on a Vertical Stabilizer and Rudder," United States Patent, 2012/0091266 A1, 2012.

[20]Whalen, E.A., Lacy, D., Lin, John C., Andino, M.Y., Washburn, A.E., Graff, E., Wygnanski, I.J., "Performance Enhancement of a Full-Scale Vertical Tail Model Equipped with Active Flow Control" AIAA-2015-0784

[21]Whalen, E.A., Khodadoust, A., "Final Report, Flight Services and Aircraft Access, NASA NAS1-NNL10AA05B TASK NNL14AA57T" The Boeing Company, August 31, 2015

[22]Woszidlo, R. and Wygnanski, I., "Parameters Governing Separation Control with Sweeping Jet Actuators," AIAA-2011-3172.